

---

# FRInGe: Distribution-Space Integrated Gradients with Fisher–Rao Geometry

---

**Gabriele Martino**

Faculty of Computer Science / Doctoral School Computer Science  
University of Vienna  
Vienna, Austria  
gabriele.martino@univie.ac.at

**Sebastian Tschitschek**

Faculty of Computer Science / ds:UniVie  
University of Vienna  
Vienna, Austria  
sebastian.tschitschek@univie.ac.at

## Abstract

Gradient-based attribution methods are model-faithful and scalable, but Integrated Gradients (IG) can be brittle because explanations depend on heuristic baselines, straight-line paths, discretization, and saturation. We propose Fisher–Rao Integrated Gradients (FRInGe), which defines both the reference and interpolation schedule in predictive distribution space. FRInGe replaces input baselines with a maximum-entropy predictive reference and follows a Fisher–Rao geodesic on the probability simplex. The corresponding input-space trajectory is realized through the pullback Fisher metric and stabilized by KL and Euclidean trust regions; attributions are obtained by integrating input gradients along this trajectory. Across six ImageNet architectures, FRInGe most clearly improves calibration-oriented attribution metrics, especially MAS scores, while remaining competitive on perturbation AUC and infidelity.

## 1 Introduction

Deep neural networks are increasingly deployed in high-stakes domains such as medical imaging and robotics, yet the rationale behind individual predictions often remains opaque. This has motivated research in explainable AI (XAI), where *feature attribution* methods aim to identify the input components most relevant for a model’s output. Among these, gradient-based approaches are particularly prominent because they are model-faithful, require only backpropagation, and scale to modern deep architectures.

A prominent representative of this family is Integrated Gradients (IG) [12]. Given an input  $x$  and a baseline  $x'$ , IG attributes importance to each feature by integrating the gradient of the model output along a path connecting  $x'$  to  $x$ . Under mild regularity assumptions, this construction satisfies desirable properties such as implementation invariance, sensitivity, and completeness.

Despite its theoretical appeal, IG can be sensitive to several practical choices. First, the *baseline* is intended to represent an absence of information, but common choices such as an all-zero image or noise can induce qualitatively different explanations [10]. Second, the *integration path*, typically chosen as a straight line in input space, can traverse regions where gradients are poorly conditioned or dominated by artifacts [1, 4, 7, 17]. Recent work has therefore explored replacing straight-line paths with geometry-aware trajectories [9]. Third, IG approximates the path integral by a finite Riemann

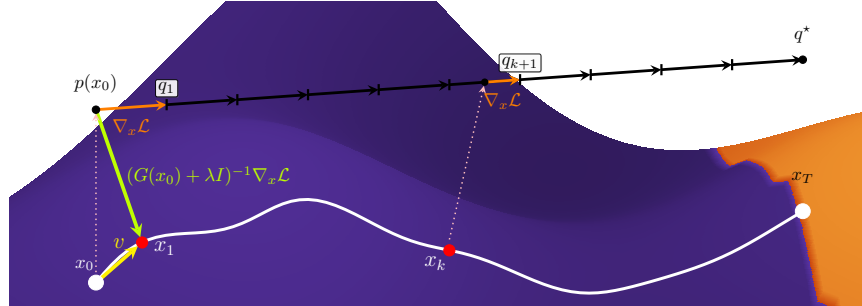


Figure 1: Visualization of the Fisher–Rao pullback metric to project the gradient toward the maximum-entropy in the input space.

sum, and the resulting discretization error can become substantial when gradients vary sharply along the path. These issues are further compounded by *saturation*: along large portions of the standard path, the model output may change rapidly early on and then plateau, so informative gradients are concentrated in a narrow segment while later integration steps contribute mostly noisy or weakly informative signal [15]. In practice, this can lead to explanations that vary with the baseline, the number of integration steps, or small implementation details.

In this paper, we address these issues by defining both the reference and the interpolation schedule in *predictive distribution space*. Rather than selecting a heuristic input-space baseline, we use a *distributional* reference point: the maximum-entropy (uniform) predictive distribution, which operationalizes “no information” directly at the model output level. We then interpolate from the model’s predictive distribution to this reference along a Fisher–Rao geodesic on the probability simplex. To realize this trajectory in input space, we use the Fisher–Rao *pullback metric*, which induces a local geometry on the input through the model’s mapping from inputs to predictive distributions. This yields a model-aware direction field that avoids committing to a Euclidean straight-line interpolation. To obtain a stable realized trajectory, we further use a trust-region step rule combining KL control in predictive space with a Euclidean cap in input space. Feature attributions are then computed by integrating input gradients along the resulting intrinsic path.

To the best of our knowledge, FRInGe is the first attribution method that (i) defines the IG reference in predictive distribution space, (ii) constructs the integration schedule as a Fisher–Rao geodesic in that space, and (iii) induces the corresponding input-space trajectory via the Fisher–Rao pullback metric. In contrast to prior path variants that design trajectories directly in input space, or methods that rely on an explicit generative model of the data manifold, our path is defined intrinsically by the geometry of the model’s predictive distribution and then lifted back to input space. Defining the reference in predictive distribution space also reduces dependence on data-type-specific baseline design.

In summary, FRInGe combines three ingredients: a maximum-entropy predictive reference replacing heuristic input-space baselines, a Fisher–Rao geodesic schedule between the model prediction and the uniform distribution, and a corresponding input-space trajectory induced by the pullback Fisher metric with trust-region stabilization. Across six ImageNet architectures and multiple attribution metrics, FRInGe shows its clearest empirical advantage on calibration-oriented attribution quality, while remaining competitive on perturbation-based AUC criteria and infidelity.

## 2 Related Work

### 2.1 Baseline choice in Integrated Gradients

A recurring practical challenge in Integrated Gradients (IG) is that the baseline is not a benign implementation detail: different baselines can yield qualitatively different explanations. Prior work has therefore sought to reduce baseline arbitrariness either by analyzing baseline sensitivity or by replacing a single reference with a distribution or a set of baselines. Sturmfels et al. [10] provide a detailed analysis of baseline sensitivity and argue that baselines encode different notions of “missingness,” motivating the use of *baseline distributions* rather than a single reference input. Expected Gradients

operationalizes this idea by averaging IG over baselines sampled from a reference distribution, typically the data distribution, thereby reducing dependence on any specific baseline and improving stability in practice [3]. A complementary line of work connects baselines to Shapley-style attributions. Sundararajan and Najmi [11] formalize how different Shapley operationalizations correspond to different reference conventions and propose *Baseline Shapley* as a principled construction. Building on this perspective, Liu et al. [5] propose Shapley Integrated Gradients (SIG), which constructs a *set* of baselines via proportional sampling to better approximate Shapley coalitions. Other approaches tailor baselines to domain semantics; for example, Bardhan et al. [1] show in particle-physics settings that averaging baselines from background events can yield more meaningful attributions than a zero reference. Recent work further argues that candidate baselines should not be treated as equally appropriate and proposes selecting or weighting them according to suitability criteria [14]. Overall, these approaches mitigate baseline dependence by averaging across baselines, constructing baseline sets, or weighting candidate references. In contrast, Tan et al. [13] argue that a principled notion of “no information” corresponds to *maximum entropy* in the model’s output distribution. We adopt this perspective by defining the reference point in *predictive distribution space*, thereby avoiding the need to specify a heuristic reference directly in input space.

## 2.2 Finding a better path

Beyond the baseline, a substantial body of work improves IG by modifying the integration path to avoid regions where gradients are unstable, saturated, or dominated by artifacts. Guided Integrated Gradients (GuidedIG) [4] attributes much of IG’s noise to the fixed Euclidean straight-line path and proposes an adaptive, model-dependent trajectory that advances preferentially along features with small partial derivatives, helping avoid high-curvature and saturation-dominated segments. Blur Integrated Gradients [16] replaces linear interpolation with a scale-space path defined by progressively blurring the input, yielding cleaner and more structured attributions through controlled information removal. Other variants modify the path more aggressively to counteract saturation or align the trajectory with decision-relevant directions. IG<sup>2</sup> [18] chains IG across intermediate baselines to smooth the attribution process, while Adversarial Gradient Integration (AGI) [6] integrates gradients along adversarially constructed trajectories that follow steepest-ascent directions in input space; related work further refines such adversarial paths to better align gradient accumulation with decision boundaries [8]. More explicitly geometric approaches have also emerged. GGIG [7] perturbs interpolants by ascending the loss landscape to emphasize discriminative directions, while Manifold Integrated Gradients (MIG) [17] integrates along geodesics of a learned data manifold induced by a deep generative model. We do not include MIG in the main benchmark because it requires an auxiliary generative model to define the data manifold. This would conflate attribution quality with generator architecture and training quality, whereas FRInGe is a model-only post-hoc method requiring only the trained classifier and automatic differentiation. Most closely related to our perspective, Salek and Enguehard [9] propose Geodesic Integrated Gradients (GeoIG), which replaces the Euclidean straight-line interpolation with geodesics in input space under a model-induced metric defined from the Jacobian, approximated either via shortest paths on a  $k$ -NN graph or via an energy-based sampling procedure. In contrast, our method does not define the path directly in input space: it defines both the reference and the interpolation schedule in *predictive distribution space* under Fisher–Rao geometry, and then realizes the corresponding input-space trajectory through the pullback metric together with trust-region stabilization. Because of this close conceptual overlap, geometry-aware path methods such as GGIG and GeoIG form especially important empirical comparators for FRInGe.

## 3 Background

Let  $F: \mathbb{R}^n \rightarrow \mathbb{R}^C$  be a differentiable model, let  $x \in \mathbb{R}^n$  denote an input, let  $C$  be the number of classes, and let  $x' \in \mathbb{R}^n$  be a baseline. Fix a target class  $t \in \{1, \dots, C\}$  and define the corresponding scalar score  $F^t: \mathbb{R}^n \rightarrow \mathbb{R}$ , for example the  $t$ -th logit.

**Integrated Gradients.** Let  $\gamma: [0, 1] \rightarrow \mathbb{R}^n$  be a  $C^1$  curve with  $\gamma(0) = x'$  and  $\gamma(1) = x$ . Integrated Gradients along  $\gamma$  is defined component-wise by

$$[\text{IG}_\gamma(x; x')]_i = \int_0^1 \frac{\partial F^t}{\partial x_i}(\gamma(\alpha)) \frac{d\gamma_i(\alpha)}{d\alpha} d\alpha, \quad (1)$$

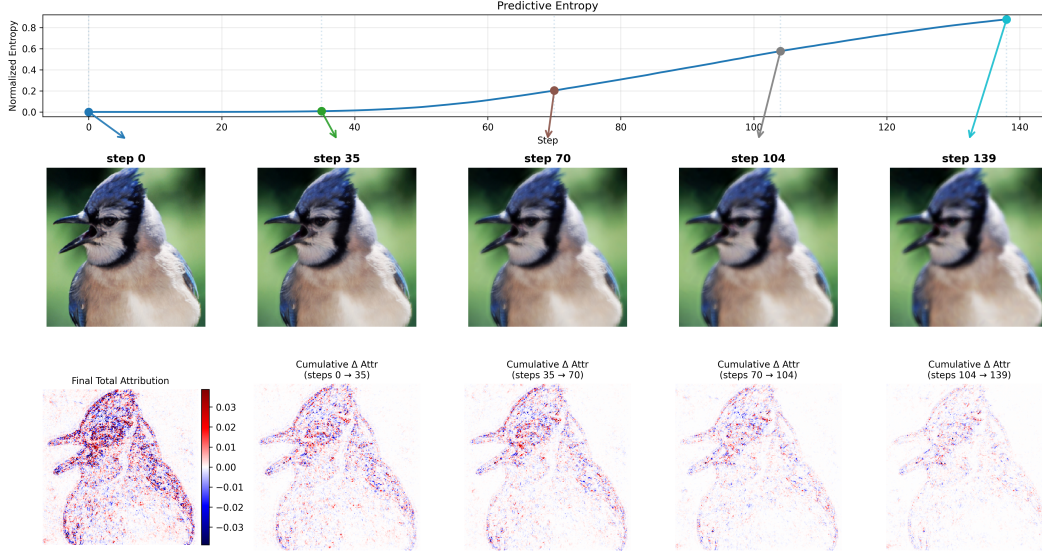


Figure 2: *Top*: normalized predictive entropy along the path. *Middle*: intermediate inputs show controlled attenuation of informative features. *Bottom*: cumulative attribution maps over equal integration eras. FRInGe concentrates attribution mass in the early, high-curvature part of the Fisher–Rao path, reducing late-stage saturation.

or equivalently in vector form

$$\text{IG}_\gamma(x; x') = \int_0^1 \nabla F^t(\gamma(\alpha)) \odot \gamma'(\alpha) d\alpha. \quad (2)$$

By the fundamental theorem for line integrals, IG satisfies *completeness*:

$$\sum_{i=1}^n [\text{IG}_\gamma(x; x')]_i = F^t(x) - F^t(x'). \quad (3)$$

In practice, the integral is approximated numerically, and the resulting discretization error can become non-negligible when gradients vary sharply or when the realized trajectory changes too abruptly between successive integration points.

**Fisher–Rao geometry and geodesics on the simplex.** Let  $F(x) \in \mathbb{R}^C$  denote the logits and let

$$p(x) = \text{softmax}(F(x)) \in \Delta^{C-1}$$

be the predictive distribution, where

$$\Delta^{C-1} = \left\{ p \in \mathbb{R}_{\geq 0}^C : \sum_{c=1}^C p_c = 1 \right\}.$$

For categorical distributions, the Fisher–Rao geometry is conveniently represented through the elementwise square-root map

$$\psi(p) = \sqrt{p},$$

which embeds the simplex into the positive orthant of the unit sphere

$$\mathbb{S}_+^{C-1} = \{ u \in \mathbb{R}_{\geq 0}^C : \|u\|_2 = 1 \}.$$

Under this embedding, Fisher–Rao geodesics on the simplex correspond to great-circle geodesics on the sphere, up to a constant rescaling of arc length.

Given two predictive distributions  $p_0, p_1 \in \Delta^{C-1}$ , define

$$\psi_0 = \sqrt{p_0}, \quad \psi_1 = \sqrt{p_1}, \quad \theta = \arccos(\langle \psi_0, \psi_1 \rangle).$$

A constant-speed shortest path on the sphere from  $\psi_0$  to  $\psi_1$  is given by the spherical linear interpolation

$$s(\alpha) = \frac{\sin((1-\alpha)\theta)}{\sin\theta} \psi_0 + \frac{\sin(\alpha\theta)}{\sin\theta} \psi_1, \quad \alpha \in [0, 1]. \quad (4)$$

Mapping this path back to the simplex yields

$$p(\alpha) = s(\alpha) \odot s(\alpha), \quad (5)$$

which is the Fisher–Rao geodesic between  $p_0$  and  $p_1$ . The corresponding Fisher–Rao distance is

$$d_{\text{FR}}(p_0, p_1) = 2 \arccos(\langle \sqrt{p_0}, \sqrt{p_1} \rangle). \quad (6)$$

**Pullback Fisher metric in input space.** Let  $J_F(x) = \partial F(x)/\partial x \in \mathbb{R}^{C \times n}$  denote the Jacobian of logits with respect to the input. For a softmax model, the Fisher information in logit coordinates is

$$S(x) = \text{diag}(p(x)) - p(x)p(x)^\top \in \mathbb{R}^{C \times C}. \quad (7)$$

The induced *pullback Fisher metric* on input space is

$$G(x) = J_F(x)^\top S(x) J_F(x) \in \mathbb{R}^{n \times n}. \quad (8)$$

This matrix is positive semidefinite and may be rank-deficient or ill-conditioned in high-dimensional settings. It provides a local quadratic approximation of the KL divergence between nearby predictive distributions:

$$\text{KL}(p(x+dx) \parallel p(x)) \approx \frac{1}{2} dx^\top G(x) dx. \quad (9)$$

## 4 Method

Let  $F : \mathbb{R}^n \rightarrow \mathbb{R}^C$  denote the logit map and let  $p(x) = \text{softmax}(F(x))$  be the predictive distribution. Given an input  $x$  and a target component  $t$ , our goal is to compute feature attributions for  $F^t(x)$  while reducing sensitivity to heuristic *input-space* baselines and to integration paths that traverse poorly behaved regions. At a high level, we define a path in *predictive distribution space* from the model prediction  $p(x)$  to a reference distribution  $q^*$ , and then realize an *input-space* trajectory whose predictive distributions approximately follow this schedule under the pullback Fisher geometry. Attributions are finally obtained by integrating input gradients along the realized input-space trajectory.

**Reference distribution.** The reference distribution  $q^* \in \Delta^{C-1}$  represents a task-dependent notion of “no evidence” or “uninformative prediction.” In this work, we adopt the maximum-entropy choice

$$q^* = u = \frac{1}{C} \mathbf{1}, \quad (10)$$

motivated by the maximum entropy principle [13]. This yields a model-agnostic reference specified directly in predictive distribution space. While we focus on the uniform distribution, other priors could be substituted when domain knowledge suggests a more appropriate uninformative target.

**Inducing an input-space trajectory that tracks predictive waypoints.** Let  $p_0 = p(x)$  denote the predictive distribution of the input, and let  $s(\alpha)$  be the Fisher–Rao geodesic in square-root coordinates defined in Eq. (4). For  $\alpha_k = k/T$ ,  $k = 0, \dots, T$ , we define the waypoint sequence

$$s_k = s(\alpha_k), \quad q_k = s_k \odot s_k, \quad (11)$$

so that  $q_0 = p_0$  and  $q_T = q^*$ . To induce a corresponding trajectory in input space, we use the spherical alignment loss

$$\mathcal{L}_k(x) = 1 - \left\langle \sqrt{p(x)}, s_k \right\rangle, \quad (12)$$

which is minimized when the current predictive distribution aligns with the target waypoint.

A Euclidean descent direction for  $\mathcal{L}_k$  would track the predictive waypoints, but it ignores the model-induced geometry and can enter poorly conditioned input-space regions. We instead use the pullback Fisher metric to obtain geometry-aware directions; this optimization only realizes the path, while attribution is still computed by path-integrated gradients.

**Geometry-aware steps via a damped natural gradient.** Let  $G(x_k)$  denote the pullback Fisher metric, cf. Eq. (8), and define the induced norm

$$\|v\|_{G(x_k)}^2 := v^\top G(x_k) v. \quad (13)$$

At waypoint  $k$ , let

$$g_k = \nabla_x \mathcal{L}_k(x)|_{x=x_k}.$$

We obtain a metric-aware descent direction by solving

$$v_k = \arg \min_{v \in \mathbb{R}^n} \left\{ \frac{1}{2} v^\top G(x_k) v + \frac{\lambda}{2} \|v\|_2^2 - g_k^\top v \right\}, \quad (14)$$

whose first-order optimality condition is

$$(G(x_k) + \lambda I) v_k = g_k. \quad (15)$$

The damping  $\lambda > 0$  is needed because  $G(x_k)$  is positive semidefinite and can be ill-conditioned. Explicitly forming  $G(x_k)$  is intractable in high dimensions, so we compute matrix-vector products implicitly using Jacobian-vector products (JVPs) and vector-Jacobian products (VJPs), and solve Eq. (15) using conjugate gradients (CG). Implementation details are given in Appendix A.4.

The resulting update has the form

$$x_{k+1} = x_k - \eta_k v_k, \quad (16)$$

where the step size  $\eta_k$  is chosen through a trust-region rule.

**Trust-region step selection in predictive and input space.** Using the local quadratic approximation in Eq. (9), we have

$$\text{KL}(p(x_k - \eta v_k) \| p(x_k)) \approx \frac{1}{2} \eta^2 \|v_k\|_{G(x_k)}^2. \quad (17)$$

Given a KL budget  $\tau > 0$ , this yields the predictive-space step bound

$$\eta_{\text{KL}} = \sqrt{\frac{2\tau}{\|v_k\|_{G(x_k)}^2 + \varepsilon}}, \quad (18)$$

with  $\varepsilon > 0$  for numerical stability. Large Fisher norm implies that even a small input displacement produces a large predictive-space change, so Eq. (18) automatically reduces the step size in high-curvature regions and allows larger steps in flatter regions.

In practice, however, large Euclidean displacements can still arise when the local predictive geometry is nearly flat. Such steps may remain admissible under the KL constraint while producing a poor numerical approximation of the realized input-space path integral. We therefore additionally impose a Euclidean trust-region cap

$$\eta_{\text{Euc}} = \frac{\delta_{\text{Euc}}}{\|v_k\|_2 + \varepsilon}, \quad \eta_k = \min(\eta_{\text{max}}, \eta_{\text{KL}}, \eta_{\text{Euc}}). \quad (19)$$

The role of  $\delta$  is thus not to improve exact predictive-space tracking, but to stabilize the realized input-space trajectory along which attributions are numerically accumulated. In particular, the Euclidean cap can trade more accurate waypoint tracking for a smaller quadrature error of the realized path integral.

**Synchronization of integration steps.** To align the nominal integration budget with the Fisher–Rao distance to the reference distribution, we set the number of waypoints using the geodesic distance from the initial prediction to the uniform target:

$$D_{\text{total}} = d_{\text{FR}}(p(x), q^*). \quad (20)$$

Under the local quadratic approximation, a constant KL step of size  $\tau$  corresponds to a nominal Riemannian arc length of approximately  $\sqrt{2\tau}$ . We therefore choose

$$T = \left\lceil \frac{D_{\text{total}}}{\sqrt{2\tau}} \right\rceil. \quad (21)$$

This synchronization should be interpreted as a nominal step-count prescription rather than an exact arrival guarantee: because the Euclidean cap in Eq. (19) can become active, the realized discrete trajectory need not reach the maximum-entropy target exactly.

**Smoothness regularization to discourage adversarial trajectories.** Matching intermediate predictive targets can admit highly non-perceptual, high-frequency input perturbations. To encourage smoother trajectories in input space and reduce susceptibility to adversarial "shortcut" paths [2], we regularize the update using a linear smoothing operator  $L$  (e.g., a discrete Laplacian). The benchmarked implementation solves

$$(G(x_k) + \lambda I + \gamma_{\text{step}} L^\top L) v_k = g_k + \gamma_{\text{prior}} L^\top L x_k. \quad (22)$$

The coefficient  $\gamma_{\text{step}}$  regularizes the update direction itself by suppressing high-frequency components in  $v_k$ , while  $\gamma_{\text{prior}}$  biases the trajectory toward smoother landing points in input space. When  $L$  is the Laplacian,  $L^\top L$  corresponds to a biharmonic operator. For exposition, the simplified case  $\gamma_{\text{step}} = \gamma_{\text{prior}}$  recovers the single-weight form. In our experiments, this regularization is particularly useful for convolutional image models, which are known to be sensitive to high-frequency perturbations.

**Attribution computation.** Finally, we approximate the IG path integral along the piecewise-linear trajectory induced by the iterates  $\{x_k\}_{k=0}^T$ . Because the trajectory is realized from the original input toward the reference, the raw accumulated path integral has the reverse orientation relative to standard baseline-to-input IG. We therefore accumulate

$$A_{\text{path}} \leftarrow A_{\text{path}} + \frac{1}{2} \left( \nabla_x F^t(x_k) + \nabla_x F^t(x_{k+1}) \right) \odot (x_{k+1} - x_k). \quad (23)$$

and return  $A = -A_{\text{path}}$ , restoring the conventional baseline-to-input attribution orientation after integrating along the reverse path. Consequently, FRInGe satisfies completeness with respect to the realized endpoint  $x_T(x)$  of its input-dependent trajectory, i.e.  $\sum_i A_i \approx F^t(x) - F^t(x_T(x))$ , rather than with respect to a fixed input-space baseline; we discuss this axiomatic status in Appendix A.6. The full procedure is given as pseudocode in Appendix A.1. Figure 2 illustrates a representative FRInGe trajectory.

**Computational complexity.** FRInGe replaces the fixed-budget path integral of standard IG with a dynamic trajectory and therefore requires an inner conjugate-gradient solve at each waypoint. In automatic differentiation frameworks, each CG iteration requires one Jacobian-vector product and one vector-Jacobian product. To ensure tractability, we truncate CG after a fixed maximum number of iterations per step. This bounds the per-step cost and, in practice, also acts as a mild regularizer against ill-conditioned high-frequency directions. A complete derivation of the total computational cost is given in Appendix A.7.

## 5 Experiments

**Experimental setup.** We evaluate FRInGe on 1,000 images randomly sampled from the ImageNet validation set. For each image, we explain the model’s top-1 predicted class. We report results on Inception-v3, ResNet-18, ResNet-50, ResNet-101, ResNet-152, and VGG-19, all using standard pretrained weights and their default preprocessing pipelines. We compare FRInGe against classical attribution baselines, including Integrated Gradients (IG), IG<sup>2</sup>, SmoothGrad, GuidedIG, and Adversarial IG, as well as geometry-aware path baselines, namely GGIG and Geodesic Integrated Gradients (GeoIG). To isolate the contribution of the main components of FRInGe, we additionally report ablations comparing Euclidean distribution tracking, unregularized Fisher-Rao tracking, and the full regularized method. Exact implementation details and hyperparameter settings are provided in the appendix. Code is available in an anonymous repository at <https://anonymous.4open.science/r/FRInGe-D5F4>.

**Evaluation protocol and metrics.** We evaluate each attribution map using four complementary criteria. First, for *causal faithfulness*, we report insertion and deletion AUC under blur-based perturbation. Second, for *attribution calibration*, we report MAS-Insertion and MAS-Deletion, which test whether cumulative attribution mass follows the corresponding change in model confidence. Unlike perturbation AUC, which mainly evaluates the induced pixel ranking, MAS also evaluates whether attribution magnitudes are calibrated to the model’s own confidence dynamics. Third, for *local robustness*, we report Infidelity and, in the appendix, Max Sensitivity under small input

Table 1: Attribution performance on representative architectures (mean  $\pm$  95% CI). Best point estimates are in **bold**.

Metric	Arch.	FRInGe	IG	SG	GGIG	GeoIG
MAS-Ins $\uparrow$	RN18	<b>0.597 <math>\pm</math> 0.015</b>	0.443 $\pm$ 0.015	0.488 $\pm$ 0.014	0.426 $\pm$ 0.016	0.453 $\pm$ 0.014
	Inc-v3	<b>0.761 <math>\pm</math> 0.009</b>	0.673 $\pm$ 0.010	0.660 $\pm$ 0.009	0.631 $\pm$ 0.011	0.647 $\pm$ 0.009
MAS-Del $\downarrow$	RN18	<b>0.264 <math>\pm</math> 0.010</b>	0.359 $\pm$ 0.011	0.325 $\pm$ 0.004	0.373 $\pm$ 0.008	0.359 $\pm$ 0.007
	Inc-v3	0.444 $\pm$ 0.020	0.485 $\pm$ 0.019	<b>0.373 <math>\pm</math> 0.008</b>	0.473 $\pm$ 0.015	0.469 $\pm$ 0.016
Ins-AUC $\uparrow$	RN18	<b>0.492 <math>\pm</math> 0.016</b>	0.415 $\pm$ 0.014	0.477 $\pm$ 0.015	0.404 $\pm$ 0.016	0.430 $\pm$ 0.014
	Inc-v3	<b>0.709 <math>\pm</math> 0.014</b>	0.647 $\pm$ 0.014	0.690 $\pm$ 0.013	0.658 $\pm$ 0.015	0.668 $\pm$ 0.014
Del-AUC $\downarrow$	RN18	0.130 $\pm$ 0.008	0.178 $\pm$ 0.010	<b>0.122 <math>\pm</math> 0.007</b>	0.164 $\pm$ 0.009	0.135 $\pm$ 0.008
	Inc-v3	0.240 $\pm$ 0.012	0.271 $\pm$ 0.013	<b>0.206 <math>\pm</math> 0.011</b>	0.215 $\pm$ 0.011	0.216 $\pm$ 0.011

perturbations. Fourth, for *explanation focus*, we report Sparseness as a descriptive measure of how concentrated each attribution map is. Full metric definitions and perturbation details are given in Appendix C.3.

## 5.1 Comparison against baseline methods

Table 1 reports a representative subset of architectures and baselines: standard IG, SmoothGrad as a strong perturbation-AUC baseline, and GGIG/GeoIG as the closest geometric competitors. Full results across all six architectures and seven baselines are provided in Appendix D.

The main pattern is that FRInGe is strongest on calibration-oriented metrics, especially MAS-Insertion. Across the full evaluation, FRInGe attains the best MAS-Insertion score on all six architectures, while MAS-Deletion ranks first on three architectures and remains competitive on the others. Figure 3 illustrates the corresponding qualitative behavior: FRInGe often yields more focused object-relevant attributions than IG or GeoIG, consistent with its stronger MAS scores.

Blur-based insertion and deletion AUC show a more mixed picture. FRInGe remains competitive and often strong on insertion, but it is not uniformly best on deletion, where smoothing-based methods such as SmoothGrad can perform better. Thus, FRInGe’s primary empirical advantage is attribution calibration rather than uniform dominance across all perturbation metrics.

The comparisons with GGIG and GeoIG are particularly important because they test whether the gains come merely from using a non-Euclidean path. Across the full evaluation, FRInGe outperforms both geometric baselines on MAS-Insertion and MAS-Deletion, and is substantially better than GeoIG on Infidelity (Appendix D). These results support the claim that FRInGe’s benefits come from the combination of a predictive-space reference, a Fisher–Rao geodesic schedule, and stabilized input-space realization, rather than from geometric path design alone.

## 5.2 Ablation study

We ablate the three main components of FRInGe: predictive-space tracking, pullback Fisher–Rao geometry, and spatial regularization. Specifically, we compare Euclidean distribution tracking, unregularized Fisher–Rao tracking, and the full regularized FRInGe objective. Full quantitative results across all architectures are reported in Table 6, with trajectory diagnostics and additional smoothing ablations in Appendix B.

The ablation results show a consistent pattern: full FRInGe is strongest on MAS-Insertion, MAS-Deletion, insertion AUC, and deletion AUC across all evaluated architectures. In contrast, the simpler Euclidean and unregularized Fisher–Rao variants often produce more sparse maps, but this additional concentration does not translate into better calibration or causal faithfulness. The qualitative trajectory diagnostics in Appendix B further clarify this behavior: Euclidean tracking and unregularized Fisher–Rao updates tend to produce high-frequency or speckled transformations, while the full regularized method yields smoother, more spatially coherent evidence removal. These results support the claim that FRInGe’s gains arise from the combination of predictive-space scheduling, pullback geometry, and spatial regularization, rather than from any single component alone.

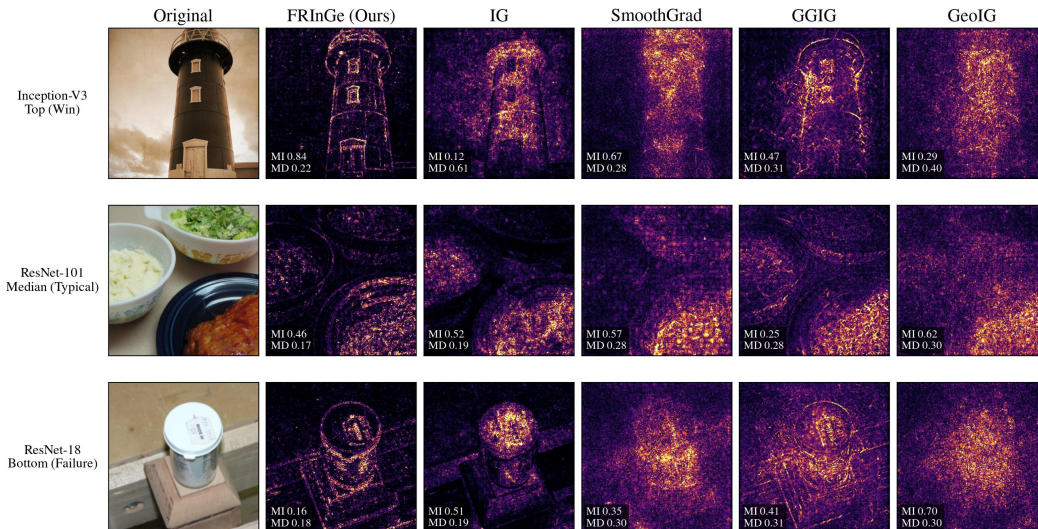


Figure 3: Qualitative comparison across architectures. We show a strong case (Inception-v3, top), a typical case (ResNet-101, middle), and a representative failure case (ResNet-18, bottom), where smoothing slightly blurs object boundaries. FRInGe yields more focused object-relevant attributions than IG or GeoIG, consistent with its stronger MAS scores. Telemetry reports image-level MAS-Insertion (MI) and MAS-Deletion (MD).

### 5.3 Hyperparameter and robustness sensitivity

The Euclidean step cap  $\delta_{\text{euc}}$  complements the KL trust region by stabilizing the realized input-space trajectory rather than improving exact predictive-space tracking. As shown in Appendix A.10, activating this cap typically reduces the realized-path completeness residual, but increases the endpoint gap to the maximum-entropy target and slightly worsens waypoint tracking. FRInGe therefore trades exact endpoint convergence for a more stable numerical approximation of the attribution integral.

We also perform one-factor-at-a-time hyperparameter sweeps over  $\delta_{\text{euc}}$ ,  $\tau$ ,  $\gamma$ ,  $\eta_{\text{max}}$ , and  $\lambda$  (Appendix C.6). The solver and step-size parameters show broad stability plateaus, while the main sensitivity lies in  $\delta_{\text{euc}}$  and  $\gamma$ , which directly control trajectory stabilization and spatial smoothing. Within moderate ranges, FRInGe preserves its calibration advantages without per-image tuning. Max Sensitivity results in Appendix D.3 and Table 13 are mixed relative to IG, reinforcing that FRInGe’s main advantage is attribution calibration rather than universal local robustness.

## 6 Discussion and Conclusion

FRInGe redefines Integrated Gradients by moving both the reference point and the interpolation schedule from input space to predictive distribution space. Rather than relying on a heuristic baseline image and a fixed Euclidean interpolation, it targets a maximum-entropy predictive reference and follows a Fisher–Rao geodesic. The corresponding input-space trajectory is realized through the pullback Fisher geometry and stabilized by KL and Euclidean trust regions together with spatial smoothing. In this sense, FRInGe measures progress by changes in the model’s predictive state, rather than by Euclidean distance in pixel space.

This perspective is reflected most clearly by the MAS-style metrics. Unlike pure ranking-based perturbation AUCs, MAS evaluates whether the accumulated attribution mass follows the actual evolution of the model’s confidence under controlled insertion or deletion. Strong MAS performance therefore indicates not only that the highlighted pixels are relevant, but also that attribution magnitudes are calibrated to the model’s predictive response. FRInGe’s strongest and most consistent gains occur precisely on these metrics, supporting the claim that the Fisher–Rao trajectory produces explanations that better track the model’s internal confidence dynamics.

More broadly, FRInGe opens a new family of geometric interpretability methods in which baselines and paths are specified in predictive distribution space rather than directly in input space. This shift removes the need to hand-design an input-space baseline for each data modality, replacing it with a distributional reference that encodes the desired predictive state. In our instantiation, this reference is the maximum-entropy prediction, and the interpolation is governed by Fisher–Rao geometry. Other predictive references, priors, or distribution-space geometries could therefore yield alternative post-hoc attribution methods while preserving the central idea: explanations should follow the model’s own predictive dynamics rather than an arbitrary Euclidean path in input space. The main practical limitation is computational cost, since FRInGe requires solving a pullback-Fisher linear system along the trajectory. In this work we control this cost by truncating CG iterations, while future work can further accelerate the method through cheaper structural approximations of the inverse pullback metric, amortized predictors of the natural-gradient direction, or more efficient implicit solvers. Overall, FRInGe offers a principled distribution-space alternative to Euclidean IG, with its central benefit being the alignment of attribution magnitude with the model’s confidence dynamics under controlled evidence removal.

## Acknowledgments and Disclosure of Funding

This work has been funded in parts by the Vienna Science and Technology Fund (WWTF) [10.47379/LS23053].

## References

- [1] Jai Bardhan, Cyrin Neeraj, Mihir Rawat, and Subhadip Mitra. Constructing sensible baselines for integrated gradients. *arXiv preprint arXiv:2412.13864*, 2024.
- [2] Ann-Kathrin Dombrowski, Maximillian Alber, Christopher Anders, Marcel Ackermann, Klaus-Robert Müller, and Pan Kessel. Explanations can be manipulated and geometry is to blame. *Advances in Neural Information Processing Systems (NeurIPS)*, 32, 2019.
- [3] Gabriel Erion, Joseph D Janizek, Pascal Sturmfels, Scott M Lundberg, and Su-In Lee. Improving performance of deep learning models with axiomatic attribution priors and expected gradients. *Nature Machine Intelligence*, 3(7):620–631, 2021.
- [4] Andrei Kapishnikov, Subhashini Venugopalan, Besim Avci, Ben Wedin, Michael Terry, and Tolga Bolukbasi. Guided integrated gradients: An adaptive path method for removing noise. In *Conference on Computer Vision and Pattern Recognition (CVPR)*, pages 5050–5058. IEEE, 2021.
- [5] Shuyang Liu, Zixuan Chen, Ge Shi, Ji Wang, Changjie Fan, Yu Xiong, Runze Wu Yujing Hu, Ze Ji, and Yang Gao. A new baseline assumption of integrated gradients based on shaply value. *arXiv preprint arXiv:2310.04821*, 2023.
- [6] Deng Pan, Xin Li, and Dongxiao Zhu. Explaining deep neural network models with adversarial gradient integration. In *International Joint Conference on Artificial Intelligence (IJCAI)*, 2021.
- [7] Md Mahfuzur Rahman, Noah Lewis, and Sergey Plis. Geometrically guided saliency maps. In *ICLR 2022 Workshop on PAIR<sup>2</sup> Struct: Privacy, Accountability, Interpretability, Robustness, Reasoning on Structured Data*, 2022.
- [8] Yuchen Ren, Zhengyu Zhao, Chenhao Lin, Bo Yang, Lu Zhou, Zhe Liu, and Chao Shen. Improving integrated gradient-based transferable adversarial examples by refining the integration path. In *Conference on Artificial Intelligence (AAAI)*, volume 39, pages 6731–6739, 2025.
- [9] Sina Salek and Joseph Enguehard. Using the path of least resistance to explain deep networks. *arXiv preprint arXiv:2502.12108*, 2025.
- [10] Pascal Sturmfels, Scott Lundberg, and Su-In Lee. Visualizing the impact of feature attribution baselines. *Distill*, 2020. <https://distill.pub/2020/attribution-baselines>.
- [11] Mukund Sundararajan and Amir Najmi. The many shapley values for model explanation. In *International Conference on Machine Learning (ICML)*, pages 9269–9278, 2020.

- [12] Mukund Sundararajan, Ankur Taly, and Qiqi Yan. Axiomatic attribution for deep networks. In *International Conference on Machine Learning (ICML)*, pages 3319–3328, 2017.
- [13] Hanxiao Tan. Maximum entropy baseline for integrated gradients. In *2023 International Joint Conference on Neural Networks (IJCNN)*, pages 1–8. IEEE, 2023.
- [14] Kien Tran Duc Tuan, Tam Nguyen Trong, Son Nguyen Hoang, Khoat Than, and Anh Nguyen Duc. Weighted integrated gradients for feature attribution. *arXiv preprint arXiv:2505.03201*, 2025.
- [15] Chase Walker, Sumit Jha, Kenny Chen, and Rickard Ewetz. Integrated decision gradients: Compute your attributions where the model makes its decision. In *Conference on Artificial Intelligence (AAAI)*, volume 38, pages 5289–5297, 2024.
- [16] Shawn Xu, Subhashini Venugopalan, and Mukund Sundararajan. Attribution in scale and space. In *Conference on Computer Vision and Pattern Recognition (CVPR)*, pages 9680–9689. IEEE, 2020.
- [17] Eslam Zaher, Maciej Trzaskowski, Quan Nguyen, and Fred Roosta. Manifold integrated gradients: Riemannian geometry for feature attribution. In *International Conference on Machine Learning (ICML)*, pages 58090–58104, 2024.
- [18] Yue Zhuo and Zhiqiang Ge. Ig 2: Integrated gradient on iterative gradient path for feature attribution. *Transactions on Pattern Analysis and Machine Intelligence (TPAMI)*, 46(11):7173–7190, 2024.

## A FRInGe Implementation Details

### A.1 FRInGe Pseudocode

---

**Algorithm 1** FRInGe
 

---

**Require:** Input  $x$ , target  $t$ , logits  $F$ ; damping  $\lambda$ , KL budget  $\tau$ , step cap  $\eta_{\max}$ , Euclidean cap  $\delta_{\text{euc}}$ ; smoothing operator  $L$  and coefficients  $\gamma_{\text{step}}, \gamma_{\text{prior}}$

**Returns:** Attributions  $A$

- 1: Compute  $T$  using Eq. (21)
  - 2:  $p_0 \leftarrow \text{softmax}(F(x)), q^* \leftarrow \frac{1}{C} \mathbf{1}$
  - 3: Build Fisher–Rao waypoints  $\{s_k\}_{k=0}^T$  between  $\sqrt{p_0}$  and  $\sqrt{q^*}$
  - 4:  $x_0 \leftarrow x, A_{\text{path}} \leftarrow 0$
  - 5: **for**  $k = 0, \dots, T - 1$  **do**
  - 6:    $p_k \leftarrow \text{softmax}(F(x_k))$
  - 7:    $\mathcal{L}_k \leftarrow 1 - \langle \sqrt{p_k}, s_k \rangle$
  - 8:    $g_k \leftarrow \nabla_x \mathcal{L}_k(x)|_{x_k}$
  - 9:   Solve  $(G_k + \lambda I + \gamma_{\text{step}} L^\top L)v_k = g_k + \gamma_{\text{prior}} L^\top L x_k$  by CG
  - 10:    $n_k^2 \leftarrow v_k^\top G_k v_k$
  - 11:    $\eta_k \leftarrow \min\left(\eta_{\max}, \sqrt{\frac{2\tau}{n_k^2 + \varepsilon}}, \frac{\delta_{\text{euc}}}{\|v_k\|_2 + \varepsilon}\right)$
  - 12:    $x_{k+1} \leftarrow x_k - \eta_k v_k$
  - 13:    $A_{\text{path}} \leftarrow A_{\text{path}} + \frac{1}{2}(\nabla_x F^t(x_k) + \nabla_x F^t(x_{k+1})) \odot (x_{k+1} - x_k)$
  - 14: **end for**
  - 15: **return**  $A = -A_{\text{path}}$
- 

### A.2 Distribution-Space Reference Path

FRInGe replaces heuristic input-space baselines with a reference defined directly in predictive distribution space. Given an input  $x_0 = x$ , let

$$p_0 = \text{softmax}(F(x_0))$$

denote the initial predictive distribution, and let

$$q^* = \frac{1}{C} \mathbf{1}$$

be the maximum-entropy reference distribution. Rather than constructing a Euclidean interpolation in input space, FRInGe builds a sequence of waypoints along the Fisher–Rao geodesic from  $p_0$  to  $q^*$ .

As described in the main text, this geodesic is most conveniently represented in square-root probability coordinates. Let

$$s(\alpha), \quad \alpha \in [0, 1],$$

denote the spherical interpolation between  $\sqrt{p_0}$  and  $\sqrt{q^*}$  given in Eq. (4). We discretize this path at

$$\alpha_k = k/T, \quad k = 0, \dots, T,$$

to obtain square-root waypoints

$$s_k = s(\alpha_k),$$

and corresponding simplex waypoints

$$q_k = s_k \odot s_k.$$

Thus,  $q_0 = p_0$  and  $q_T = q^*$ . These waypoints define the sequence of predictive targets that the induced input-space trajectory attempts to follow.

At waypoint  $k$ , the implementation uses the spherical alignment loss

$$\mathcal{L}_k(x) = 1 - \langle \sqrt{p(x)}, s_k \rangle,$$

whose gradient attracts the current prediction toward the next Fisher–Rao waypoint. Consequently, although the state of the algorithm evolves in input space, the nominal direction and step schedule are governed by the geometry of the predictive distribution, before stabilization by the input-space trust region.

### A.3 Pullback Fisher Geometry

To transfer the Fisher–Rao geometry of the simplex back to the input domain, FRInGe uses the pullback Fisher metric induced by the model. Let

$$p(x) = \text{softmax}(F(x)),$$

and let

$$J_F(x) = \frac{\partial F(x)}{\partial x} \in \mathbb{R}^{C \times n}$$

denote the Jacobian of logits with respect to the input. The Fisher information matrix in logit coordinates is

$$S(x) = S(p(x)) = \text{diag}(p(x)) - p(x)p(x)^\top.$$

The pullback Fisher metric in input space is then

$$G(x) = J_F(x)^\top S(p(x)) J_F(x).$$

In high-dimensional vision settings, the dense matrix  $G(x)$  is never explicitly materialized. Instead, FRInGe computes matrix-vector products with  $G(x)$  implicitly. For any vector  $v$ ,

$$G(x)v = J_F(x)^\top (S(p(x))(J_F(x)v)).$$

Operationally, this is implemented by:

1. a Jacobian-vector product (JVP) to compute  $J_F(x)v$ ,
2. multiplication by the analytic softmax Fisher matrix  $S(p(x))$ ,
3. a vector-Jacobian product (VJP) to map the result back to input space.

This matrix-free implementation is the key step that makes the method computationally feasible for image-sized inputs.

### A.4 Regularized Linear System, Decoupled Smoothing, and Sobolev Preconditioning

At each waypoint  $k$ , FRInGe computes an update direction  $v_k$  by solving a regularized linear system of the form

$$(G(x_k) + \lambda I + \gamma_{\text{step}} L^\top L)v_k = g_k + \gamma_{\text{prior}} L^\top L x_k,$$

where

$$g_k = \nabla_x \mathcal{L}_k(x_k),$$

$\lambda > 0$  is a Tikhonov damping coefficient, and  $L$  is a spatial smoothing operator, typically chosen as a discrete Laplacian. In this case,  $L^\top L$  is a biharmonic operator.

This implementation refines the simplified single- $\gamma$  presentation used in the main text. The two smoothing coefficients play distinct roles:

- $\gamma_{\text{step}}$  appears on the left-hand side and regularizes the update direction itself. It suppresses high-frequency components in  $v_k$  and improves the conditioning of the linear system.
- $\gamma_{\text{prior}}$  appears on the right-hand side and injects a spatial prior from the current state  $x_k$ . Its main effect is to bias the trajectory away from high-frequency perturbations already present in the current iterate.

When  $\gamma_{\text{step}} = \gamma_{\text{prior}} = \gamma$ , the system reduces to the simplified regularized formulation described in the main text.

The resulting system is solved using preconditioned conjugate gradients (PCG). Because the dominant numerical difficulty comes from poorly conditioned high-frequency directions, we use a Sobolev-style preconditioner in the smoothed setting. In the implementation, the action of  $M^{-1}$  is approximated by Gaussian blurring followed by scaling by  $1/\lambda$ :

$$M^{-1}(v) \approx \frac{\text{Blur}(v)}{\lambda}.$$

This should not be interpreted as an exact inverse of the biharmonic operator. Rather, it is an empirical preconditioner that attenuates the high-frequency modes most responsible for slow CG convergence and yields a substantial practical speedup. When smoothing is disabled, the preconditioner reduces to the simple diagonal scaling

$$M^{-1}(v) = \frac{v}{\lambda}.$$

The implementation also warm-starts PCG using the solution from the previous waypoint. Since consecutive linear systems are close along the trajectory, this significantly reduces the number of iterations required in practice and improves solver stability.

### A.5 Attribution Quadrature and Sign Convention

The benchmarked implementation accumulates attributions along the induced input-space trajectory using a trapezoidal rule rather than a purely left-point discretization. Let  $F^t(x)$  denote the target score used for attribution accumulation. The path integral is updated as

$$A_{\text{path}} \leftarrow A_{\text{path}} + \frac{1}{2} \left( \nabla_x F^t(x_k) + \nabla_x F^t(x_{k+1}) \right) \odot (x_{k+1} - x_k).$$

This discretization is more accurate than a one-sided Riemann sum and matches the implementation used in our experiments.

Because FRInGe evolves the state from the original input toward the reference trajectory, the raw accumulated path integral satisfies

$$\sum_i A_{\text{path},i} \approx F^t(x_T) - F^t(x_0).$$

This is the reverse of the conventional baseline-to-input orientation used in standard Integrated Gradients. To return attributions in the usual sign convention, the implementation outputs

$$A = -A_{\text{path}}.$$

This sign flip is essential rather than cosmetic: it is also the reason the completeness check in the code is written against the forward path orientation actually followed during optimization.

### A.6 Axiomatic Status and Realized-Path Completeness

FRInGe should be interpreted as an Integrated-Gradients line integral along an input-dependent realized path, rather than as standard IG with a fixed input-space baseline. For each input  $x$ , the algorithm constructs a trajectory  $\gamma_x : [0, 1] \rightarrow \mathbb{R}^n$  with  $\gamma_x(0) = x$  and  $\gamma_x(1) = x_T(x)$ , where  $x_T(x)$  is the endpoint reached by the trust-region dynamics. In the continuous limit, the FRInGe attribution is

$$A_{\text{FRInGe}}(x) = - \int_0^1 \nabla_x F^t(\gamma_x(\alpha)) \odot \gamma'_x(\alpha) d\alpha.$$

Therefore,

$$\sum_i A_{\text{FRInGe},i}(x) = F^t(x) - F^t(x_T(x)).$$

Thus, FRInGe preserves completeness with respect to the realized endpoint of its own trajectory. It does not claim classical fixed-baseline completeness with respect to an input-independent baseline  $x'$ . This is a deliberate change: the reference is specified in predictive distribution space, while the corresponding input-space endpoint is obtained by the stabilized pullback dynamics.

In the implemented method, the reported completeness residual measures only the finite-step quadrature error along this realized path. Separately, the endpoint KL reported in Appendix A.10 measures how close the realized endpoint prediction is to the ideal maximum-entropy reference. These two quantities capture different effects: numerical accuracy of the path integral and proximity to the intended predictive-space reference.

FRInGe retains implementation invariance in the following functional sense: two implementations that realize the same differentiable logit map  $F$  along the trajectory induce the same predictive distributions, pullback metric, path, and line-integral attribution. However, since the path depends on the full predictive distribution, methods that agree only on the scalar target score  $F^t$  but not on the full logit map need not yield identical FRInGe paths.

## A.7 Computational Complexity Analysis

We analyze the computational cost of FRInGe relative to standard Integrated Gradients (IG). Let  $C_{\text{fwd}}$  and  $C_{\text{bwd}}$  denote the costs of a forward and backward pass, respectively. In modern automatic differentiation frameworks, a JVP has cost comparable to  $C_{\text{fwd}}$ , while a VJP has cost comparable to  $C_{\text{bwd}}$ .

Standard IG with  $N$  integration steps requires one forward and one backward pass per step to evaluate  $\nabla_x F^t(x)$ , giving total cost

$$C_{\text{IG}} = N(C_{\text{fwd}} + C_{\text{bwd}}).$$

FRInGe uses a dynamic number of waypoints  $T$  together with an inner CG loop. Up to lower-order initialization costs, each waypoint requires:

1. one forward pass to evaluate  $p(x_k)$ ,
2. one backward pass to compute the waypoint-tracking gradient  $g_k = \nabla_x \mathcal{L}_k(x_k)$ ,
3. one backward pass for attribution accumulation along the path,
4.  $K$  matrix-vector products with the pullback Fisher operator, where each product requires one JVP and one VJP.

Thus, an approximate total cost for FRInGe is

$$C_{\text{FRInGe}} \approx T[(1 + K)C_{\text{fwd}} + (2 + K)C_{\text{bwd}}].$$

Assuming  $C_{\text{fwd}} \approx C_{\text{bwd}}$ , the relative overhead scales as

$$\frac{C_{\text{FRInGe}}}{C_{\text{IG}}} \approx \frac{T}{N}(K + 1.5).$$

**Worst-Case Estimate for  $T$ .** Because  $T$  is determined from the Fisher–Rao distance to the reference distribution, it is useful to derive an upper bound. The worst case occurs when the initial prediction is maximally confident, i.e., effectively one-hot, and the target is the maximum-entropy center of the simplex,

$$q^* = \left[\frac{1}{C}, \dots, \frac{1}{C}\right].$$

The corresponding maximum Fisher–Rao arc length is

$$D_{\text{max}} = 2 \arccos(\langle \sqrt{p}, \sqrt{q^*} \rangle) = 2 \arccos\left(\frac{1}{\sqrt{C}}\right).$$

Since the KL trust-region budget  $\tau$  corresponds to a nominal arc length of approximately  $\sqrt{2\tau}$ , the worst-case step count is bounded by

$$T_{\text{max}} = \left\lceil \frac{2 \arccos(1/\sqrt{C})}{\sqrt{2\tau}} \right\rceil.$$

As  $C \rightarrow \infty$ ,  $\arccos(1/\sqrt{C}) \rightarrow \pi/2$ , so the maximum geodesic distance is bounded by  $\pi$ . Hence

$$\lim_{C \rightarrow \infty} T_{\text{max}} = \left\lceil \frac{\pi}{\sqrt{2\tau}} \right\rceil.$$

This shows that the nominal number of steps remains bounded even for large-scale classification problems such as ImageNet.

**Runtime–Fidelity Trade-off.** The computational cost of FRInGe is governed primarily by two hyperparameters: the maximum number of CG iterations  $K$  and the KL trust-region budget  $\tau$ . The parameter  $K$  controls the quality of the approximate natural-gradient solve, while  $\tau$  determines the resolution of the integration path. Smaller values of  $\tau$  increase the number of waypoints and reduce discretization error, but also increase runtime. Conversely, larger values of  $\tau$  reduce the number of steps at the cost of a coarser approximation to the Fisher–Rao trajectory.

In practice,  $K$  acts as a ceiling rather than a fixed per-step cost. Because the solver is warm-started and preconditioned, convergence often occurs in substantially fewer than  $K$  iterations. Consequently,  $K$  and  $\tau$  provide a transparent mechanism for trading computational cost against geometric accuracy.

**Empirical Runtime Comparison with Integrated Gradients.** To complement the asymptotic complexity analysis with a practical estimate, we benchmark FRInGe against standard Integrated Gradients (IG) on 64 ImageNet images under sequential execution. All runtime measurements were performed on NVIDIA H100 GPUs using the same software environment and preprocessing pipeline for both methods. In this comparison, IG batching is disabled to isolate the intrinsic per-image algorithmic overhead of the two methods. Table 2 shows that FRInGe is consistently slower than standard IG, as expected from the additional pullback-Fisher linear solves performed along the trajectory.

This overhead is the main practical cost of the proposed geometry-aware path construction. At the same time, the reported runtimes remain compatible with offline attribution analysis, where explanations are computed after training or for selected validation, audit, or debugging samples rather than in a real-time inference loop. Reducing this cost through structured approximations of the pullback metric, amortized natural-gradient predictors, or more efficient implicit solvers is an important direction for future work.

Table 2: Sequential runtime benchmark on 64 images. Times are mean seconds  $\pm$  95% CI. IG batching is disabled to isolate sequential algorithmic cost.

Model	FRInGe (s)	IG (s)	Slowdown
ResNet-18	55.12 $\pm$ 0.80	2.90 $\pm$ 0.01	19.0 $\times$
ResNet-50	45.00 $\pm$ 0.41	9.53 $\pm$ 0.03	4.7 $\times$
ResNet-101	228.21 $\pm$ 1.58	11.59 $\pm$ 0.04	19.7 $\times$
ResNet-152	319.21 $\pm$ 2.89	15.28 $\pm$ 0.01	20.9 $\times$
Inception-v3	159.80 $\pm$ 3.58	14.94 $\pm$ 0.03	10.7 $\times$
VGG-19	43.65 $\pm$ 0.58	1.95 $\pm$ 0.01	22.3 $\times$

## A.8 Trust-Region Step Selection

Once the direction  $v_k$  has been computed, FRInGe chooses a step size that respects both the local Fisher geometry and a Euclidean cap in input space. The implemented rule is

$$\eta_k = \min\left(\eta_{\max}, \sqrt{\frac{2\tau}{\|v_k\|_{G(x_k)}^2 + \varepsilon}}, \frac{\delta_{\text{euc}}}{\|v_k\|_2 + \varepsilon}\right),$$

where  $\tau$  is the KL-based trust-region budget,  $\eta_{\max}$  is a global maximum step size,  $\delta_{\text{euc}}$  is the Euclidean trust-region radius, and  $\varepsilon > 0$  is a numerical stability constant.

The corresponding update is  $x_{k+1} = x_k - \eta_k v_k$ . The Fisher–Rao term controls motion in predictive distribution space by approximately enforcing a constant local KL budget, while the Euclidean cap prevents excessively large displacements in pixel space. In practice, the minimum of these constraints is more stable than either constraint alone.

Because the Euclidean cap can become active, the discrete trajectory need not reach the reference distribution exactly even when  $T$  is chosen from the nominal Fisher–Rao arc length. This explains why the synchronization rule for  $T$  should be interpreted as a nominal step-count prescription rather than a guarantee of exact arrival.

## A.9 Geometric Effect of the Euclidean Trust-Region Cap

To clarify the practical role of the Euclidean trust-region radius  $\delta_{\text{euc}}$ , we compare the geometric profiles of three trajectories: standard IG, FRInGe without the Euclidean cap, and FRInGe with the full trust-region rule. Figure 4 reports, for each path, the per-step change in predictive distribution measured in the pullback Fisher geometry, the corresponding Euclidean step size in input space, and the evolution of predictive entropy along the trajectory.

The standard IG profile in Fig. 4c illustrates the central limitation of the classical straight-line interpolation: the Euclidean step size is constant by construction, but the induced progress in predictive space is highly non-uniform. In particular, the Fisher–Rao step remains close to zero for most of the trajectory and rises sharply only near the endpoint, while the predictive entropy increases

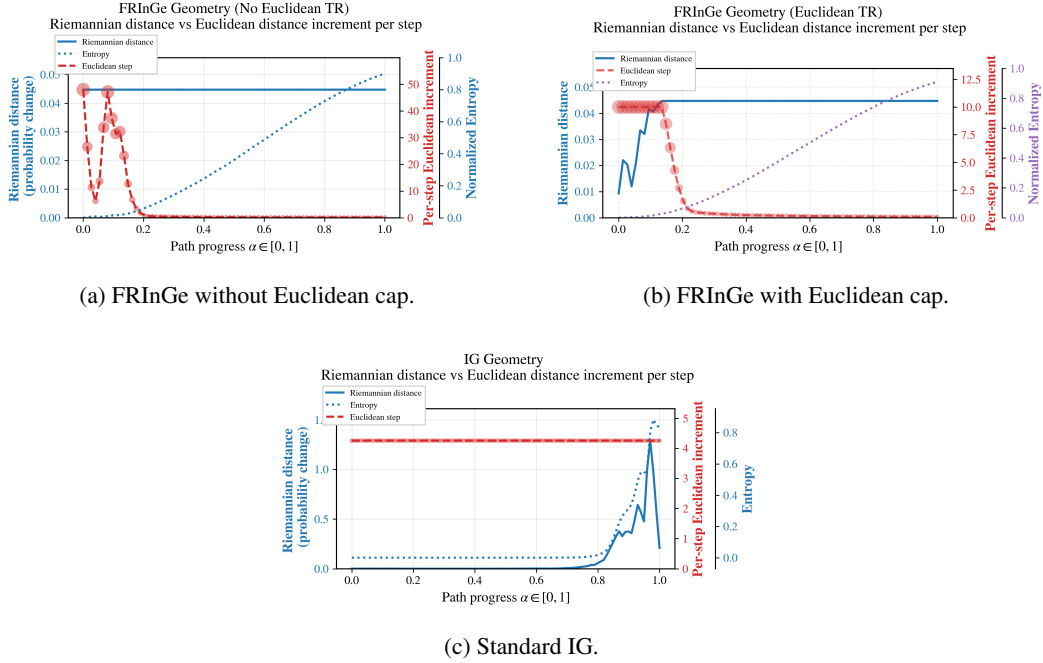


Figure 4: Geometric profiles of the integration trajectory. **Top left:** FRInGe without the Euclidean trust-region cap maintains nearly constant progress in predictive space, but can require very large Euclidean displacements early in the trajectory. **Top right:** activating the Euclidean cap suppresses these large early jumps; in the initial part of the path the Euclidean constraint is active, while later the KL-based trust region becomes the limiting factor and the Riemannian step becomes approximately constant. **Bottom:** standard IG uses constant Euclidean steps by construction, but the predictive distribution changes only weakly over most of the path, leading to a late increase in entropy and illustrating the classical saturation problem.

only late in the path. This is precisely the *saturation problem* often discussed in the Integrated Gradients literature: a large fraction of the path contributes little meaningful change in model output, and many subsequent variants of IG have been motivated by the need to overcome this inefficiency.

The unbounded FRInGe profile in Fig. 4a shows the opposite regime. Once the trajectory is driven by a KL-controlled rule in predictive space, the induced Fisher–Rao step becomes nearly constant and entropy increases much more smoothly, indicating a more uniform removal of predictive information along the path. However, the Euclidean step required to maintain this approximately constant Riemannian step can become extremely large when the local geometry is nearly flat. In the example shown here, the Euclidean step norm reaches values of about 50, which is substantial enough to compromise the numerical approximation of the path integral and motivate an additional input-space stabilization mechanism.

This is exactly the role of the Euclidean cap in Fig. 4b. When  $\delta_{\text{euc}}$  is activated, the Euclidean step is visibly clipped at the beginning of the trajectory and remains approximately constant at the prescribed value of 10, reflecting the fact that the Euclidean trust region is active in this regime. Later along the path, once the KL constraint becomes more restrictive than the Euclidean one, the Riemannian step becomes the active constant quantity instead. The resulting trajectory therefore combines the two regimes: early stabilization in input space through the Euclidean cap, followed by controlled predictive-space progress under the KL trust region. This visual comparison makes clear that the Euclidean cap should not be interpreted as improving exact waypoint tracking; rather, its purpose is to stabilize the numerical realization of the path along which attributions are accumulated. This qualitative behavior is consistent with the quantitative trade-off reported in Appendix A.10, where activating  $\delta_{\text{euc}}$  reduces the completeness residual of the realized integral while generally worsening predictive-space waypoint tracking.

### A.10 Quantitative Effect of the Euclidean Trust-Region Cap

The Euclidean trust-region radius  $\delta_{\text{euc}}$  introduces a deliberate trade-off between predictive-space waypoint tracking and numerical stability of the realized input-space trajectory. To make this trade-off explicit, we report two complementary diagnostics.

First, we evaluate the *realized-path completeness residual*, measured with respect to the endpoint actually reached by the discrete trajectory:

$$\varepsilon_{\text{comp}} = \frac{|\sum_i A_i - (F^t(x_0) - F^t(x_T))|}{|F^t(x_0) - F^t(x_T)| + \varepsilon}.$$

This quantity measures how closely the numerically accumulated attribution satisfies completeness along the realized path. Alongside it, we report the final endpoint KL

$$\text{KL}(p(x_T) \parallel u),$$

which quantifies how far the realized endpoint remains from the ideal maximum-entropy target in predictive space. These two quantities capture different aspects of the trajectory: the first concerns numerical faithfulness of the realized path integral, whereas the second concerns proximity to the intended predictive-space reference.

Second, we quantify predictive-space waypoint tracking by measuring the Fisher–Rao distance between the realized predictive distribution and the intended geodesic waypoint:

$$\varepsilon_{\text{track},k} = d_{\text{FR}}(p(x_k), q_k).$$

We summarize this tracking error using both its mean and its maximum over the trajectory.

Tables 3 and 4 show a consistent pattern across models. Activating  $\delta_{\text{euc}}$  often reduces the completeness residual of the realized input-space integral, but it also tends to increase the final endpoint KL and to worsen predictive-space waypoint tracking. The Euclidean cap should therefore be interpreted as a stabilizer of the realized integration path rather than as a mechanism for exact nonlinear shooting toward the reference distribution.

Table 3: Effect of the Euclidean trust-region cap on realized-path completeness and endpoint mismatch. Lower completeness residual is better. Lower endpoint KL indicates closer agreement with the ideal maximum-entropy target.

Model	Completeness error $\delta_{\text{euc}}$ on	Completeness error $\delta_{\text{euc}}$ off	Endpoint KL $\delta_{\text{euc}}$ on	Endpoint KL $\delta_{\text{euc}}$ off
ResNet-18	<b>0.011 ± 0.003</b>	0.078 ± 0.034	3.697 ± 0.605	<b>0.148 ± 0.030</b>
ResNet-50	<b>0.417 ± 0.174</b>	0.535 ± 0.168	2.749 ± 0.473	<b>2.435 ± 0.474</b>
ResNet-101	<b>0.184 ± 0.061</b>	0.313 ± 0.108	2.096 ± 0.530	<b>1.439 ± 0.383</b>
ResNet-152	<b>0.208 ± 0.070</b>	0.239 ± 0.071	1.235 ± 0.328	<b>1.161 ± 0.288</b>
VGG-19	<b>0.014 ± 0.005</b>	0.258 ± 0.360	4.707 ± 0.603	<b>0.188 ± 0.088</b>

Table 4: Effect of the Euclidean trust-region cap on predictive-space waypoint tracking. Lower values indicate closer agreement between the realized trajectory and the intended Fisher–Rao waypoint sequence.

Model	Mean tracking error $\delta_{\text{euc}}$ on	Mean tracking error $\delta_{\text{euc}}$ off	Max tracking error $\delta_{\text{euc}}$ on	Max tracking error $\delta_{\text{euc}}$ off
ResNet-18	0.197 ± 0.022	<b>0.046 ± 0.008</b>	0.977 ± 0.015	<b>0.850 ± 0.088</b>
ResNet-50	0.154 ± 0.017	<b>0.141 ± 0.017</b>	0.563 ± 0.083	<b>0.540 ± 0.087</b>
ResNet-101	0.145 ± 0.035	<b>0.124 ± 0.035</b>	0.859 ± 0.073	<b>0.817 ± 0.086</b>
ResNet-152	0.093 ± 0.014	<b>0.090 ± 0.013</b>	0.711 ± 0.099	<b>0.700 ± 0.101</b>
VGG-19	0.254 ± 0.024	<b>0.054 ± 0.014</b>	0.917 ± 0.035	<b>0.556 ± 0.119</b>

## B Ablation Study Configurations

To disentangle the contributions of predictive-space tracking, pullback geometry, and spatial regularization, we evaluate three progressively richer variants of the method.

**Euclidean Distribution Tracking.** This baseline tracks the same predictive-space waypoints but ignores the pullback geometry entirely. The update direction is simply

$$v_k = g_k.$$

Thus, the method follows the gradient of the spherical alignment loss directly, without Fisher conditioning, damping, or PCG. This isolates the effect of using a distribution-space target without geometric regularization.

Fig. 5 illustrates the trajectory induced by the pure Entropy Ascent update. The top panel reports the normalized predictive entropy together with selected intermediate waypoints along the path. The bottom panel shows the final attribution map and, for each displayed waypoint, the normalized blur-change map relative to the initial image, highlighting where the trajectory is acting in input space. This diagnostic confirms that the entropy-ascent direction is followed overall, although the path exhibits noisy local corrections. At the same time, the intermediate images remain visually almost unchanged, which is consistent with the discussion that, without spatial regularization, the update is dominated by high-frequency perturbations rather than perceptually meaningful transformations. The blur-change maps further indicate that the trajectory does affect regions containing informative features, but the resulting updates are highly speckled and do not integrate into a meaningful final attribution map.

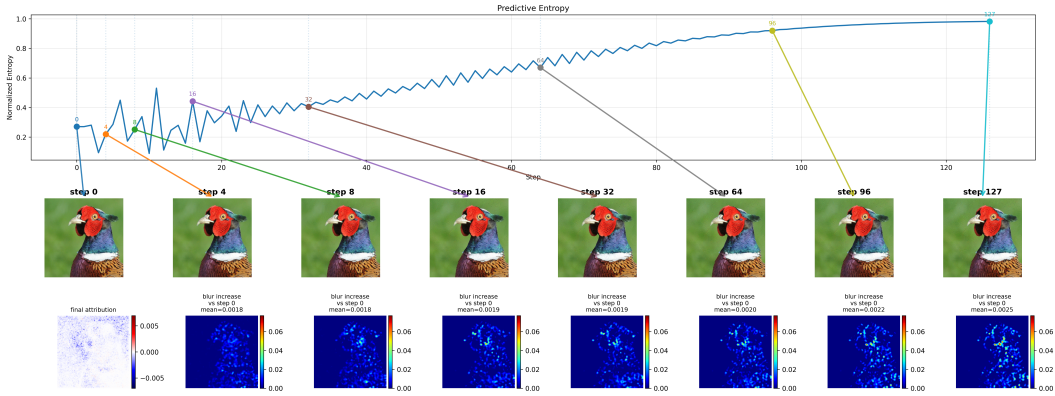


Figure 5: Example trajectory of Euclidean Distribution Tracking on ResNet-18.

**Unregularized Fisher–Rao Geometry.** This variant uses the pullback Fisher metric and solves

$$(G(x_k) + \lambda I)v_k = g_k.$$

It therefore incorporates the model-induced geometry and the KL-based trust region, but no explicit spatial smoothing. This isolates the effect of Fisher–Rao conditioning alone and reveals both its geometric faithfulness and its sensitivity to high-frequency perturbations.

Fig. 6 shows the trajectory induced by Unregularized FRInGe. In contrast to Fig. 5, the normalized predictive entropy now increases much more smoothly, which is consistent with the Fisher–Rao geometry and KL-based trust-region control producing a more coherent path in predictive space. At the same time, the intermediate images still exhibit highly localized, speckled changes, as also reflected by the blur-change maps. This indicates that, although the geometric update substantially improves the global trajectory compared with pure Entropy Ascent, the absence of an explicit spatial prior still leaves the path dominated by high-frequency perturbations. Consequently, the final attribution map remains noisy, motivating the need for the additional regularization used in the full FRInGe formulation.

**Fisher–Rao Geometry with Sobolev Smoothing (Full FRInGe).** The full method solves

$$(G(x_k) + \lambda I + \gamma_{\text{step}} L^\top L)v_k = g_k + \gamma_{\text{prior}} L^\top Lx_k,$$

together with the Sobolev-style blur preconditioner described above. This configuration combines predictive-space geometry with an explicit low-frequency spatial prior, producing substantially more stable and visually coherent attribution trajectories on high-dimensional image manifolds.

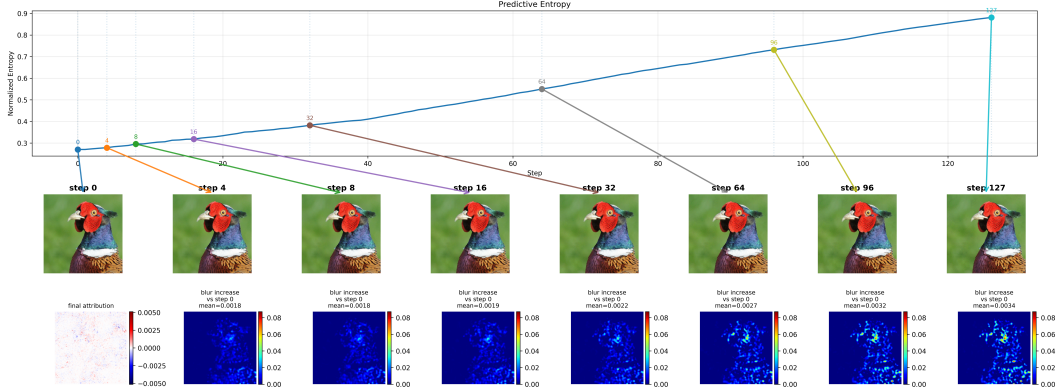


Figure 6: Example trajectory of Unregularized FRInGe on ResNet-18 model.

Fig. 7 shows the trajectory induced by the full regularized FRInGe formulation. As expected, the normalized predictive entropy increases smoothly along the path. In contrast to the previous ablations, the blur-change maps now reveal a much more structured and spatially coherent evolution: the regularization causes the induced smoothing to concentrate on the image regions most affected by the maximum-entropy direction, rather than producing diffuse high-frequency perturbations. In this example, the trajectory progressively attenuates the visual evidence in the regions that most strongly support the model’s prediction, appears to increase entropy by attenuating informative visual evidence used by the classifier. This leads to a substantially more interpretable path and a cleaner final attribution map than either the pure Entropy Ascent or the unregularized variant.

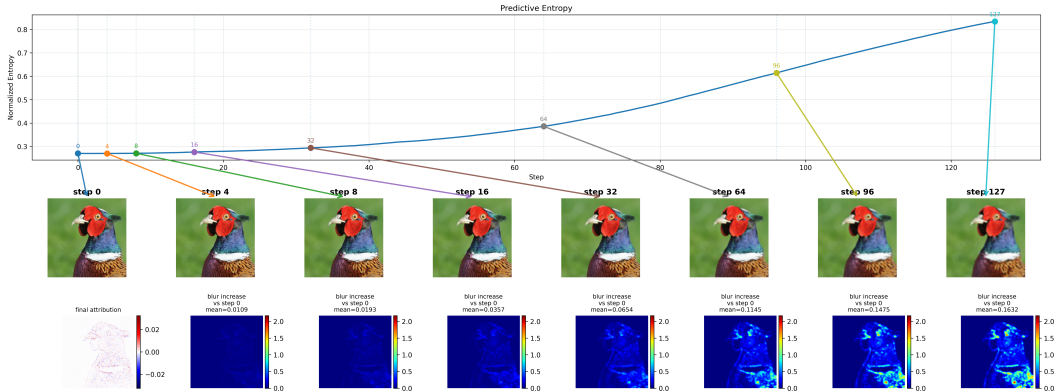


Figure 7: Example trajectory of full FRInGe on ResNet-18 model.

**On the role of  $\gamma_{\text{step}}$  and  $\gamma_{\text{prior}}$ .** The full regularized FRInGe update can be written as

$$(G(x_k) + \lambda I + \gamma_{\text{step}} L^\top L) v_k = g_k + \gamma_{\text{prior}} L^\top L x_k.$$

The two regularization terms play complementary roles. The left-hand term, controlled by  $\gamma_{\text{step}}$ , regularizes the *direction field* by penalizing high-frequency components of  $v_k$ ; empirically, this mainly stabilizes the geometry-aware update and yields a smoother entropy trajectory. The right-hand term, controlled by  $\gamma_{\text{prior}}$ , acts instead on the *transformed input*, biasing each update toward smoother landing points. This is particularly important because the subsequent attribution accumulation requires evaluating  $\nabla_x F^t(x_k)$  along the realized path, and these gradients become substantially more stable when the intermediate images evolve in a spatially coherent way.

To disentangle these effects, we visualize three additional ablations. With  $\gamma_{\text{step}}$  **only** (Fig. 8), the entropy increases smoothly, confirming that direction regularization stabilizes the predictive-space trajectory. However, the blur-change maps remain weak and speckled, and the final attribution map is still noisy. This indicates that smoothing the direction alone is not sufficient to obtain meaningful input-space transformations. With  $\gamma_{\text{prior}}$  **only inside FRInGe** (Fig. 9), the blur-change maps become

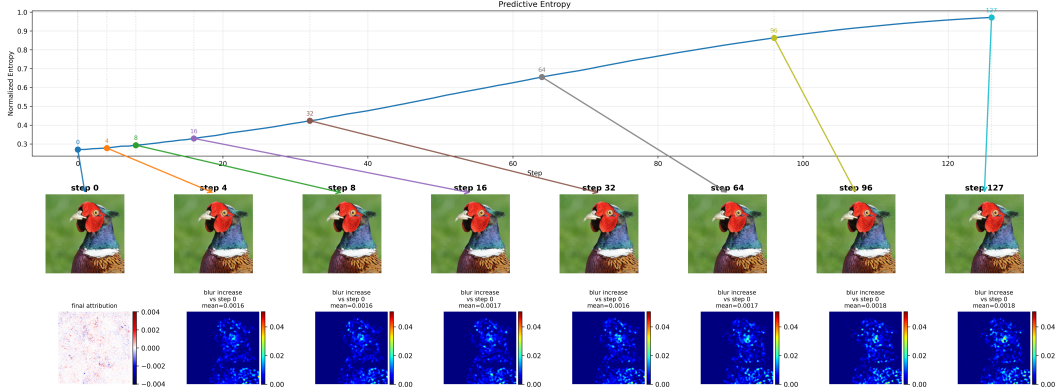


Figure 8: Trajectory induced by FRInGe with  $\gamma_{\text{step}} > 0$  and  $\gamma_{\text{prior}} = 0$  on ResNet-18. The predictive entropy evolves smoothly, indicating that regularizing the direction field stabilizes the geometry-aware path. However, the blur-change maps remain sparse and speckled, and the final attribution map is still noisy, showing that direction regularization alone is insufficient to produce meaningful input-space transformations.

much more spatially coherent and concentrate on semantically meaningful regions of the image, but the entropy evolves much more slowly, showing that input regularization alone does not provide the same predictive-space progress as the full method.

Finally, to verify that the benefits do not reduce to simply adding  $\gamma_{\text{prior}}$  to a non-geometric update, we also consider the variant

$$v_k = \nabla_x \mathcal{L}_k + \gamma_{\text{prior}} L^\top L x_k.$$

As shown in Fig. 10, this variant already produces blur maps that visually focus on informative regions, but the final attribution map remains dominated by noise. This is the key control experiment: it shows that  $\gamma_{\text{prior}}$  alone can make the intermediate transformations look more structured, but without the Fisher-aware solve the resulting attribution is still poor. Taken together, these ablations support the claim that the effectiveness of FRInGe comes from the *combination* of geometry-aware tracking, direction regularization, and input-space prior, rather than from smoothing alone.

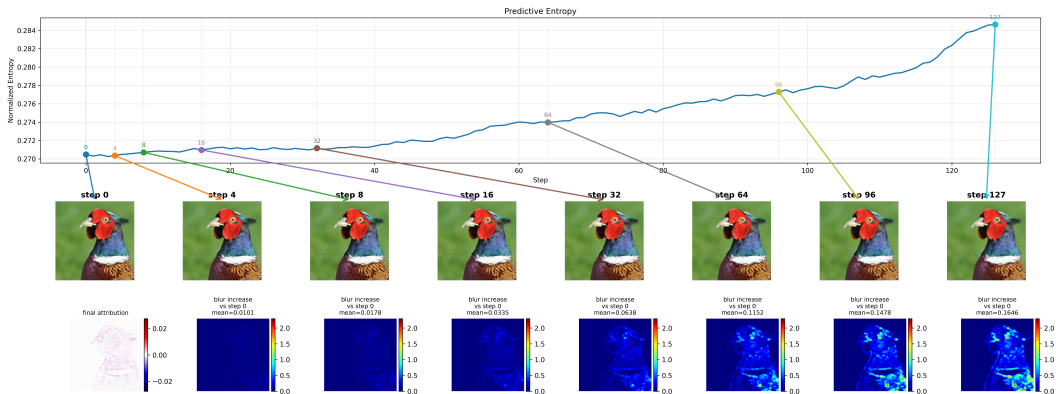


Figure 9: Trajectory induced by FRInGe with  $\gamma_{\text{step}} = 0$  and  $\gamma_{\text{prior}} > 0$  on ResNet-18. In this case, the blur-change maps become much more spatially coherent and concentrate on semantically meaningful regions, showing that  $\gamma_{\text{prior}}$  regularizes the transformed input effectively. At the same time, the entropy increases only weakly, indicating that this term alone does not provide the same predictive-space progress as the full method.

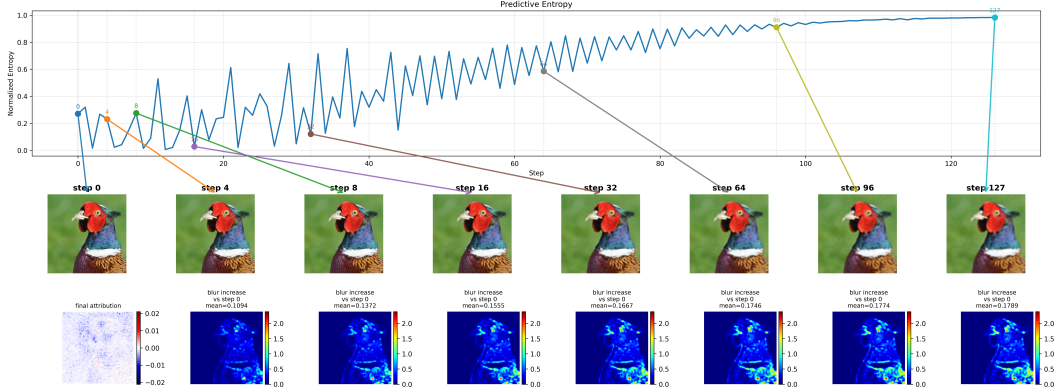


Figure 10: Trajectory induced by the non-geometric variant  $v_k = \nabla_x \mathcal{L}_k + \gamma_{\text{prior}} L^\top L x_k$  on ResNet-18. Although the blur-change maps already focus on informative image regions, the final attribution map remains largely noisy. This control experiment shows that the benefits of FRInGe do not arise from  $\gamma_{\text{prior}}$  alone, but from its interaction with the Fisher-aware geometry and the regularized solve.

## C Experimental Protocol and Reproducibility

### C.1 Dataset, Models, and Target Selection

All experiments are conducted on a benchmark of 1,000 images randomly sampled from the ImageNet validation set. We evaluate pretrained standard vision architectures together with their official preprocessing pipelines. For each image  $x$ , we explain the model’s top-1 prediction on the unperturbed input,

$$t = \arg \max_c F_c(x),$$

and keep this target fixed throughout all attribution and evaluation steps. This removes variance due to changing target labels across methods and ensures that all methods are compared on exactly the same explanation task.

Unless otherwise stated, all FRInGe results reported in the manuscript use the full regularized configuration, i.e., predictive-distribution tracking under the pullback Fisher metric together with damping, trust-region control, and Sobolev-style spatial regularization. This is the default configuration underlying all main-text results and the full-method entries in the appendix tables.

### C.2 Evaluation Pipeline and Statistical Reporting

For each image and attribution method, we compute an attribution tensor  $A \in \mathbb{R}^{3 \times H \times W}$  for the fixed target class  $t$ . These attribution maps are then evaluated using four families of metrics: causal faithfulness, attribution calibration, local robustness, and explanation focus. Since several of these evaluations require converting a channel-wise attribution tensor into a spatial ranking and then applying a perturbation protocol, we define all metrics explicitly below.

All reported confidence intervals are 95% bootstrap confidence intervals computed over images. Throughout the appendix, higher is better for MAS-Ins, Ins-AUC, and Sparseness, while lower is better for MAS-Del, Del-AUC, and Infidelity.

### C.3 Metric Definitions

#### C.3.1 Spatial Saliency Reduction

Metrics based on progressive perturbations require a spatial ranking rather than a channel-wise attribution tensor. Given  $A \in \mathbb{R}^{3 \times H \times W}$ , we define the spatial saliency map

$$S_{ij} = \max_{c \in \{1,2,3\}} |A_{cij}|,$$

where  $S_{ij}$  is the saliency assigned to pixel  $(i, j)$ . Pixels are ranked in descending order of  $S_{ij}$ , and this ranking is used in all perturbation-based evaluations.

### C.3.2 Causal Faithfulness: Blur-Based Insertion and Deletion AUC

All perturbations are defined relative to a blurred reference image  $x_{\text{blur}}$ , obtained by average pooling with stride 1, same padding, and kernel size

$$k = \max\left(3, \text{odd}\left(\left\lfloor \frac{\min(H, W)}{10} \right\rfloor\right)\right).$$

At perturbation step  $s$ , let  $x_s$  be the perturbed image and

$$c_s = \text{softmax}(F(x_s))_t$$

the target-class confidence. The insertion and deletion scores are then obtained as the area under the confidence curve  $\{c_s\}$ , computed with the trapezoidal rule. Intuitively, insertion measures how quickly confidence is recovered when important pixels are restored, while deletion measures how quickly confidence drops when important pixels are removed.

We also report a normalized version of the perturbation curve:

$$\tilde{c}_s = \text{clip}\left(\frac{c_s - p_{\text{blur}}}{\max(p_{\text{orig}} - p_{\text{blur}}, \varepsilon)}, 0, 1\right),$$

where

$$p_{\text{orig}} = \text{softmax}(F(x))_t, \quad p_{\text{blur}} = \text{softmax}(F(x_{\text{blur}}))_t.$$

Here,  $p_{\text{orig}}$  is the target confidence on the original image,  $p_{\text{blur}}$  is the confidence on the blurred baseline, and  $\varepsilon > 0$  is a numerical stability constant. This normalization removes dependence on the absolute confidence gap between the original and blurred images.

### C.3.3 Magnitude Aligned Scoring (MAS)

MAS evaluates whether the *magnitude* of the attribution is aligned with the actual evolution of model confidence during perturbation. Given a spatial ranking, MAS defines three quantities.

First, the *Density Response*

$$DR_k = \frac{\sum_{i=0}^k |A_i|}{\sum_i |A_i| + \varepsilon}$$

measures how much attribution mass has been accumulated up to perturbation step  $k$ .

Second, the *Model Response*

$$MR_k = \text{softmax}(F(X_k))_t$$

is the target-class confidence on the perturbed image  $X_k$  at the same step. In implementation, this response is normalized to  $[0, 1]$  under the same perturbation schedule.

Third, the *Alignment Penalty*

$$AP_k = |MR_k - DR_k|$$

measures the discrepancy between the fraction of attribution mass selected and the fraction of confidence recovered or removed.

The final MAS scores are

$$MAS^{\text{ins}} = \frac{1}{N} \sum_{i=0}^N MR_i^{\text{ins}} - \frac{1}{N} \sum_{i=0}^N AP_i^{\text{ins}},$$

$$MAS^{\text{del}} = \frac{1}{N} \sum_{i=0}^N MR_i^{\text{del}} + \frac{1}{N} \sum_{i=0}^N AP_i^{\text{del}}.$$

In the insertion score, the first term rewards large model response and the second penalizes misalignment between response and attribution density. In the deletion score, the penalty is added because a good explanation should remove confidence while remaining aligned with attribution mass. Higher  $MAS^{\text{ins}}$  and lower  $MAS^{\text{del}}$  indicate better-calibrated explanations.

For MAS, the perturbation baseline is a Gaussian blur with kernel size  $15 \times 15$  and standard deviation  $\sigma = 3.0$ .

### C.3.4 Local Robustness: Infidelity

Infidelity measures how well an attribution predicts the change in target score under small random perturbations. For attribution  $\Phi(x)$  and perturbation  $\delta$ , it is defined as

$$\mathbb{E}_\delta \left[ \left( \delta^\top \Phi(x) - (F^t(x) - F^t(x - \delta)) \right)^2 \right].$$

The first term,  $\delta^\top \Phi(x)$ , is the attribution-predicted score variation under perturbation  $\delta$ , while the second term is the actual change in model output. Lower infidelity indicates better local faithfulness. We estimate this expectation by Monte Carlo sampling with 50 Gaussian perturbations per image, each drawn with standard deviation  $\sigma = 0.02$ .

### C.3.5 Explanation Focus: Sparseness

We quantify explanation focus using the Gini index of the absolute attribution values. Given an attribution tensor  $A \in \mathbb{R}^{C \times H \times W}$ , we first flatten it and take absolute values:

$$a = (|A_1|, \dots, |A_n|) \in \mathbb{R}_{\geq 0}^n, \quad n = C \cdot H \cdot W.$$

Let  $a_{(1)} \leq a_{(2)} \leq \dots \leq a_{(n)}$  denote these values sorted in ascending order. The sparseness score is then computed as

$$\text{Sparseness}(A) = \frac{2 \sum_{i=1}^n i a_{(i)}}{n \sum_{i=1}^n a_{(i)} + \varepsilon} - \frac{n+1}{n},$$

where  $\varepsilon > 0$  is a small numerical stability constant. In implementation, the result is clipped to the interval  $[0, 1]$ .

This score is the Gini index of the attribution magnitude distribution. Values near 0 indicate a diffuse or nearly uniform attribution map, whereas values near 1 indicate that attribution mass is concentrated on a small number of entries. This metric is reported only as a complementary descriptive statistic and is not used directly in the causal-faithfulness or calibration evaluations above.

### C.3.6 Local Robustness: Max Sensitivity

We additionally report Max Sensitivity as a robustness diagnostic under small input perturbations. For a given input  $x$ , fixed target class  $t$ , and attribution method  $\Phi$ , we compute the attribution map and normalize it by its  $\ell_2$  norm so that the score reflects changes in explanation structure rather than overall scale:

$$\widehat{\Phi}(x) = \frac{\Phi(x)}{\|\Phi(x)\|_2 + \varepsilon}.$$

We then sample perturbations  $\delta^{(1)}, \dots, \delta^{(M)}$  independently, with entries drawn uniformly from  $[-r, r]$ , and recompute the normalized attribution for each perturbed input. In our experiments,  $r = 0.02$  and  $M = 10$ . The reported score is

$$\text{MaxSens}(x) = \max_{m=1, \dots, M} \frac{\left\| \widehat{\Phi}(x) - \widehat{\Phi}(x + \delta^{(m)}) \right\|_2}{\|\delta^{(m)}\|_2 + \varepsilon}.$$

Lower values indicate greater local robustness. Since the maximum is taken over a finite Monte Carlo sample, this is a sampled approximation of local sensitivity rather than an exact worst-case bound.

## C.4 Hyperparameter Selection Protocol

For each architecture and ablation setting, FRInGe hyperparameters were selected using Optuna on a fixed subset of 256 images. The search space included the trust-region parameters  $\tau$ ,  $\eta_{\max}$ , and  $\delta_{\text{euc}}$ , the damping coefficient  $\lambda$ , and, when smoothing was enabled, the regularization coefficients  $\gamma_{\text{step}}$  and  $\gamma_{\text{prior}}$ .

The optimization objective was a weighted harmonic mean of three quantities: blur-based insertion AUC, inverted blur-based deletion AUC, and an infidelity-derived fidelity score. Let InsAUC and

DelAUC denote the insertion and deletion AUC values on the tuning subset, and let Inf denote the infidelity score. We define

$$\text{Fid} = \exp(-k \text{Inf}), \quad k = 2,$$

and optimize

$$\text{Score} = \frac{w_{\text{ins}} + w_{\text{del}} + w_{\text{fid}}}{\frac{w_{\text{ins}}}{\text{InsAUC} + \varepsilon} + \frac{w_{\text{del}}}{(1 - \text{DelAUC}) + \varepsilon} + \frac{w_{\text{fid}}}{\text{Fid} + \varepsilon}},$$

with weights

$$w_{\text{ins}} = 1, \quad w_{\text{del}} = 1, \quad w_{\text{fid}} = 0.5,$$

and  $\varepsilon = 10^{-6}$ . This objective favors configurations that perform consistently across insertion, deletion, and local robustness, while penalizing settings that improve one quantity at the expense of the others.

### C.5 Architecture-Specific Hyperparameters

Table 5 reports the exact hyperparameter values used for each architecture and ablation configuration. These configurations are defined by the presence or absence of specific operators in the FRInGe update rather than by arbitrary cosmetic variants. In particular, the **Euclidean Tracking** baseline bypasses the linear system entirely, so damping, smoothing, and CG-related quantities are inapplicable. The **Unregularized Fisher–Rao** variant uses the pullback Fisher metric and trust-region step selection but disables spatial regularization. The **Full FRInGe** variant uses the complete regularized system described in Appendix A.4. Parameters that are mathematically inapplicable to a given variant are marked with an em dash (—). Evaluation constants unrelated to FRInGe optimization, such as perturbation schedules and Monte Carlo sample counts for the metrics, are kept fixed across models and configurations.

Table 5: Hyperparameter configurations for the ablation study. Dashes indicate parameters that are not applicable to the corresponding simplified variant.

Model	Variant	$\tau$	$\eta_{\text{max}}$	$\delta_{\text{euc}}$	$\lambda$	$\gamma_{\text{step}}$	$\gamma_{\text{prior}}$	$K$
ResNet-18	Euclidean	—	29.57503	—	—	—	—	—
	Unreg. Fisher–Rao	$3.0281 \times 10^{-4}$	1.98215	34.51936	$2.7685 \times 10^{-11}$	—	—	20
	Full FRInGe	$3.0339 \times 10^{-4}$	13.56315	0.61337	$4.7707 \times 10^{-11}$	$9.9739 \times 10^{-3}$	$9.7495 \times 10^{-4}$	20
ResNet-50	Euclidean	—	29.7014	—	—	—	—	—
	Unreg. Fisher–Rao	$3.2063 \times 10^{-4}$	1.12726	18.32001	$1.2843 \times 10^{-10}$	—	—	20
	Full FRInGe	$2.7031 \times 10^{-3}$	1.179	5.00773	$2.5802 \times 10^{-4}$	$9.943 \times 10^{-3}$	$9.4855 \times 10^{-4}$	20
ResNet-101	Euclidean	—	29.12752	—	—	—	—	—
	Unreg. Fisher–Rao	$6.4322 \times 10^{-4}$	1.017	14.4785	$1.1241 \times 10^{-12}$	—	—	20
	Full FRInGe	$3.693 \times 10^{-4}$	1.53481	3.84629	$8.0172 \times 10^{-8}$	$9.9812 \times 10^{-3}$	$6.0812 \times 10^{-4}$	20
ResNet-152	Euclidean	—	0.19345	—	—	—	—	—
	Unreg. Fisher–Rao	$3.2924 \times 10^{-4}$	1.05996	26.34784	$3.1488 \times 10^{-10}$	—	—	20
	Full FRInGe	$4.1281 \times 10^{-4}$	1.74774	3.31598	$7.5483 \times 10^{-5}$	$6.0553 \times 10^{-3}$	$9.1604 \times 10^{-4}$	20
Inception-v3	Euclidean	—	6.28255	—	—	—	—	—
	Unreg. Fisher–Rao	$1.9717 \times 10^{-3}$	2.8069	3.27511	$9.7873 \times 10^{-3}$	—	—	20
	Full FRInGe	$5.3427 \times 10^{-4}$	16.91726	24.18139	$7.1733 \times 10^{-6}$	$9.727 \times 10^{-3}$	$3.4298 \times 10^{-4}$	20
VGG-19	Euclidean	—	0.01817	—	—	—	—	—
	Unreg. Fisher–Rao	$3.2232 \times 10^{-4}$	1.11244	9.38604	$2.1686 \times 10^{-12}$	—	—	20
	Full FRInGe	$3.0449 \times 10^{-4}$	2.75362	0.6969	$3.0302 \times 10^{-11}$	$5.132 \times 10^{-3}$	$9.6205 \times 10^{-4}$	20

### C.6 Hyperparameter Sensitivity Across Architectures

To complement the architecture-specific operating points reported in Table 5, we also performed a one-factor sensitivity analysis over the main FRInGe hyperparameters. Figure 11 reports the resulting aggregated objective across all evaluated architectures while varying one hyperparameter at a time and keeping the others fixed. The objective is the same weighted harmonic-mean score used during hyperparameter selection. For the smoothing parameter, the sweep varies the regularization strength jointly, i.e.,  $\gamma_{\text{step}} = \gamma_{\text{prior}} = \gamma$ , in order to provide a compact summary of smoothing sensitivity across models.

Several patterns are consistent across architectures. First,  $\eta_{\max}$  is largely insensitive over the tested range, suggesting that it behaves primarily as a safety upper bound rather than as a performance-critical control parameter. Second,  $\tau$  is comparatively stable but not completely neutral, which is expected since it directly controls the nominal number of integration steps and therefore the resolution of the realized trajectory. Third,  $\lambda$  has a weaker and more architecture-dependent effect, consistent with its role as a conditioning parameter for the linear solve rather than as a primary geometric control.

The strongest sensitivities arise for  $\delta_{\text{euc}}$  and  $\gamma$ . The Euclidean trust-region radius acts as the main numerical stabilization parameter: if it is too small, the method becomes overly conservative and progresses slowly; if it is too large, the local path realization becomes less stable and the quality of the integral approximation degrades. The smoothing strength  $\gamma$  shows a clear beneficial effect up to a moderate range, after which improvements tend to plateau. This is consistent with the role of spatial regularization in suppressing high-frequency perturbations while preserving the large-scale geometry of the trajectory.

Taken together, these sweeps support the practical configuration used throughout the paper:  $\eta_{\max}$  can be treated as a permissive upper bound,  $\tau$  should be chosen in a moderately stable range,  $\delta_{\text{euc}}$  should be tuned as the main trust-region parameter, and  $\lambda$  should be interpreted primarily as a conditioning parameter for the CG solve. For image models in particular, moderate nonzero smoothing is consistently beneficial.

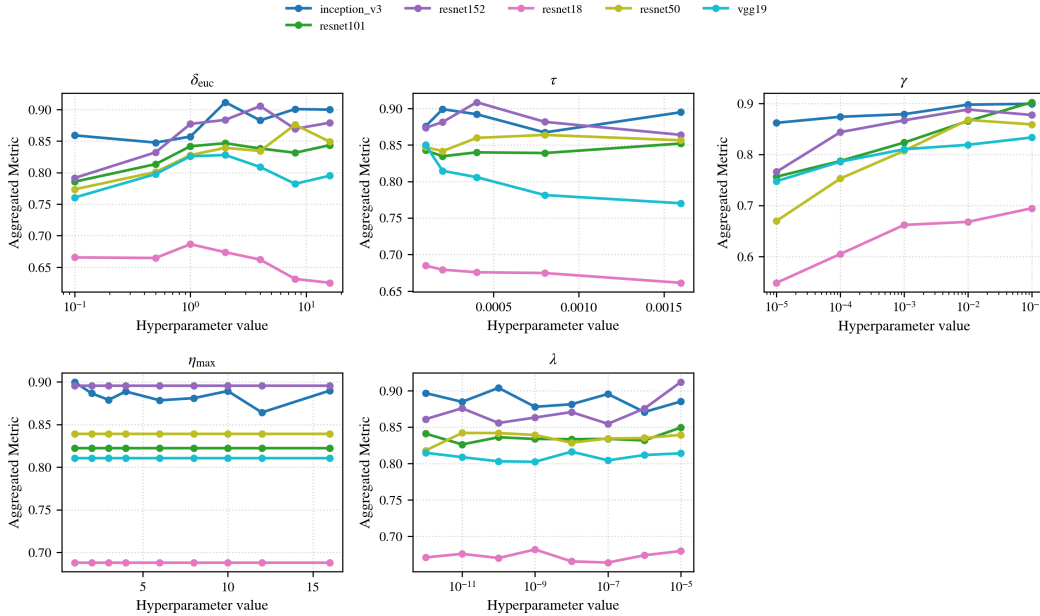


Figure 11: Sensitivity analysis of FRInGe hyperparameters across all evaluated architectures. Each panel varies one hyperparameter while keeping the others fixed and reports the aggregated tuning objective. For the smoothing sweep, we vary the regularization strength jointly, setting  $\gamma_{\text{step}} = \gamma_{\text{prior}} = \gamma$ .

## D Additional Quantitative Results

In the following tables, we report dataset-level means together with 95% bootstrap confidence intervals. For insertion and deletion, we report normalized blur-based scores in the main comparison tables, while the ablation table follows the same metric conventions used in the main text. The top-performing method in each row is highlighted in **bold**. Methods whose confidence intervals overlap with the best are highlighted in **bold** as a descriptive near-tie heuristic.

### D.1 Ablation Study

Table 6: Ablation study of FRInGe components across evaluated architectures. **Euclidean Tracking** ignores manifold curvature, **Unregularized Fisher–Rao** projects onto the manifold without spatial smoothing, and **Full FRInGe** utilizes the complete Sobolev-preconditioned system. Best results are highlighted in **bold**. Methods whose confidence intervals overlap with the best are highlighted in **bold** as a descriptive near-tie heuristic.

Metric	Euclidean Tracking	Unregularized Fisher–Rao	Full FRInGe (Ours)
<b>ResNet-18</b>			
MAS-Ins AUC $\uparrow$	0.414 $\pm$ 0.017	0.399 $\pm$ 0.017	<b>0.597 <math>\pm</math> 0.015</b>
MAS-Del AUC $\downarrow$	0.319 $\pm$ 0.012	0.330 $\pm$ 0.012	<b>0.264 <math>\pm</math> 0.010</b>
Ins-AUC $\uparrow$	0.358 $\pm$ 0.014	0.347 $\pm$ 0.013	<b>0.492 <math>\pm</math> 0.016</b>
Del-AUC $\downarrow$	0.195 $\pm$ 0.010	0.207 $\pm$ 0.010	<b>0.130 <math>\pm</math> 0.008</b>
Sparseness Score $\uparrow$	0.764 $\pm$ 0.003	<b>0.785 <math>\pm</math> 0.003</b>	0.706 $\pm$ 0.002
Infidelity Score $\downarrow$	<b>0.058 <math>\pm</math> 0.008</b>	<b>0.058 <math>\pm</math> 0.008</b>	<b>0.058 <math>\pm</math> 0.008</b>
<b>ResNet-50</b>			
MAS-Ins AUC $\uparrow$	0.491 $\pm$ 0.018	0.477 $\pm$ 0.018	<b>0.648 <math>\pm</math> 0.014</b>
MAS-Del AUC $\downarrow$	0.361 $\pm$ 0.014	0.372 $\pm$ 0.014	<b>0.302 <math>\pm</math> 0.012</b>
Ins-AUC $\uparrow$	0.415 $\pm$ 0.014	0.403 $\pm$ 0.014	<b>0.581 <math>\pm</math> 0.016</b>
Del-AUC $\downarrow$	0.246 $\pm$ 0.012	0.261 $\pm$ 0.012	<b>0.161 <math>\pm</math> 0.009</b>
Sparseness Score $\uparrow$	0.763 $\pm$ 0.003	<b>0.791 <math>\pm</math> 0.004</b>	0.702 $\pm$ 0.002
Infidelity Score $\downarrow$	<b>0.149 <math>\pm</math> 0.050</b>	<b>0.149 <math>\pm</math> 0.050</b>	<b>0.150 <math>\pm</math> 0.050</b>
<b>ResNet-101</b>			
MAS-Ins AUC $\uparrow$	0.568 $\pm$ 0.017	0.554 $\pm$ 0.018	<b>0.679 <math>\pm</math> 0.014</b>
MAS-Del AUC $\downarrow$	0.421 $\pm$ 0.017	0.432 $\pm$ 0.017	<b>0.351 <math>\pm</math> 0.015</b>
Ins-AUC $\uparrow$	0.499 $\pm$ 0.015	0.488 $\pm$ 0.015	<b>0.641 <math>\pm</math> 0.017</b>
Del-AUC $\downarrow$	0.309 $\pm$ 0.014	0.321 $\pm$ 0.014	<b>0.228 <math>\pm</math> 0.012</b>
Sparseness Score $\uparrow$	0.772 $\pm$ 0.003	<b>0.795 <math>\pm</math> 0.004</b>	0.706 $\pm$ 0.002
Infidelity Score $\downarrow$	<b>0.121 <math>\pm</math> 0.022</b>	<b>0.121 <math>\pm</math> 0.022</b>	<b>0.121 <math>\pm</math> 0.022</b>
<b>ResNet-152</b>			
MAS-Ins AUC $\uparrow$	0.591 $\pm$ 0.017	0.581 $\pm$ 0.018	<b>0.691 <math>\pm</math> 0.013</b>
MAS-Del AUC $\downarrow$	0.451 $\pm$ 0.018	0.464 $\pm$ 0.018	<b>0.392 <math>\pm</math> 0.017</b>
Ins-AUC $\uparrow$	0.531 $\pm$ 0.015	0.519 $\pm$ 0.015	<b>0.681 <math>\pm</math> 0.016</b>
Del-AUC $\downarrow$	0.351 $\pm$ 0.014	0.362 $\pm$ 0.014	<b>0.265 <math>\pm</math> 0.013</b>
Sparseness Score $\uparrow$	0.779 $\pm$ 0.003	<b>0.799 <math>\pm</math> 0.004</b>	0.703 $\pm$ 0.002
Infidelity Score $\downarrow$	<b>0.111 <math>\pm</math> 0.020</b>	<b>0.111 <math>\pm</math> 0.020</b>	<b>0.111 <math>\pm</math> 0.020</b>
<b>Inception-v3</b>			
MAS-Ins AUC $\uparrow$	0.688 $\pm$ 0.015	0.681 $\pm$ 0.015	<b>0.761 <math>\pm</math> 0.009</b>
MAS-Del AUC $\downarrow$	<b>0.467 <math>\pm</math> 0.019</b>	<b>0.483 <math>\pm</math> 0.019</b>	<b>0.444 <math>\pm</math> 0.020</b>
Ins-AUC $\uparrow$	0.580 $\pm$ 0.013	0.557 $\pm$ 0.013	<b>0.709 <math>\pm</math> 0.014</b>
Del-AUC $\downarrow$	0.300 $\pm$ 0.013	0.315 $\pm$ 0.013	<b>0.240 <math>\pm</math> 0.012</b>
Sparseness Score $\uparrow$	0.763 $\pm$ 0.003	<b>0.801 <math>\pm</math> 0.003</b>	0.723 $\pm$ 0.003
Infidelity Score $\downarrow$	<b>0.020 <math>\pm</math> 0.005</b>	<b>0.020 <math>\pm</math> 0.005</b>	<b>0.020 <math>\pm</math> 0.005</b>
<b>VGG-19</b>			
MAS-Ins AUC $\uparrow$	0.427 $\pm$ 0.017	0.413 $\pm$ 0.017	<b>0.588 <math>\pm</math> 0.015</b>
MAS-Del AUC $\downarrow$	0.319 $\pm$ 0.012	0.329 $\pm$ 0.012	<b>0.255 <math>\pm</math> 0.008</b>
Ins-AUC $\uparrow$	0.389 $\pm$ 0.015	0.382 $\pm$ 0.015	<b>0.503 <math>\pm</math> 0.016</b>
Del-AUC $\downarrow$	0.193 $\pm$ 0.010	0.204 $\pm$ 0.010	<b>0.119 <math>\pm</math> 0.007</b>
Sparseness Score $\uparrow$	<b>0.807 <math>\pm</math> 0.003</b>	<b>0.814 <math>\pm</math> 0.006</b>	0.707 $\pm$ 0.003
Infidelity Score $\downarrow$	<b>0.343 <math>\pm</math> 0.064</b>	<b>0.343 <math>\pm</math> 0.064</b>	<b>0.343 <math>\pm</math> 0.064</b>

## D.2 Comparison across attribution methods

Table 7: Quantitative evaluation on Inception-v3. Values are dataset-level mean $\pm$ 95% confidence intervals. We report only blur-based metrics for attribution calibration and causal faithfulness. Abbreviations: AGI = Adversarial IG, SG = SmoothGrad. The best result in each row is shown in **bold**; methods whose confidence intervals overlap with the best are shown in **bold**.

Metric	FRInGe (Ours)	AGI	GGIG	GeoIG	GuidedIG	IG	IG <sup>2</sup>	SG
<i>Attribution calibration</i>								
MAS-Ins $\uparrow$	<b>0.761<math>\pm</math>0.009</b>	0.605 $\pm$ 0.011	0.631 $\pm$ 0.011	0.647 $\pm$ 0.009	0.701 $\pm$ 0.010	0.673 $\pm$ 0.010	0.691 $\pm$ 0.013	0.660 $\pm$ 0.009
MAS-Del $\downarrow$	<b>0.444<math>\pm</math>0.020</b>	0.520 $\pm$ 0.017	0.473 $\pm$ 0.015	0.469 $\pm$ 0.016	0.452 $\pm$ 0.019	0.485 $\pm$ 0.019	0.455 $\pm$ 0.019	<b>0.373<math>\pm</math>0.008</b>
<i>Causal faithfulness (normalized, blur)</i>								
Ins-AUC $\uparrow$	<b>0.709<math>\pm</math>0.014</b>	0.573 $\pm$ 0.014	0.658 $\pm$ 0.015	0.668 $\pm$ 0.014	0.675 $\pm$ 0.013	0.647 $\pm$ 0.014	0.596 $\pm$ 0.013	<b>0.690<math>\pm</math>0.013</b>
Del-AUC $\downarrow$	<b>0.240<math>\pm</math>0.012</b>	0.321 $\pm$ 0.013	<b>0.215<math>\pm</math>0.011</b>	<b>0.216<math>\pm</math>0.011</b>	0.242 $\pm$ 0.013	0.271 $\pm$ 0.013	0.289 $\pm$ 0.013	<b>0.206<math>\pm</math>0.011</b>
<i>Map focus and local robustness</i>								
Sparseness $\uparrow$	0.723 $\pm$ 0.003	0.514 $\pm$ 0.006	0.471 $\pm$ 0.004	0.529 $\pm$ 0.002	0.665 $\pm$ 0.003	0.624 $\pm$ 0.003	<b>0.739<math>\pm</math>0.003</b>	0.540 $\pm$ 0.003
Infidelity $\downarrow$	<b>0.020<math>\pm</math>0.005</b>	<b>0.021<math>\pm</math>0.005</b>	0.411 $\pm$ 0.018	$4.76 \times 10^3 \pm 2.09 \times 10^2$	<b>0.027<math>\pm</math>0.005</b>	0.032 $\pm$ 0.006	<b>0.020<math>\pm</math>0.005</b>	<b>0.021<math>\pm</math>0.005</b>

Table 8: Quantitative evaluation on ResNet-18. Values are dataset-level mean $\pm$ 95% confidence intervals. We report only blur-based metrics for attribution calibration and causal faithfulness. Abbreviations: AGI = Adversarial IG, SG = SmoothGrad. The best result in each row is shown in **bold**; methods whose confidence intervals overlap with the best are shown in **bold**.

Metric	FRInGe (Ours)	AGI	GGIG	GeoIG	GuidedIG	IG	IG <sup>2</sup>	SG
<i>Attribution calibration</i>								
MAS-Ins $\uparrow$	<b>0.597<math>\pm</math>0.015</b>	0.387 $\pm$ 0.014	0.426 $\pm$ 0.016	0.453 $\pm$ 0.014	0.477 $\pm$ 0.016	0.443 $\pm$ 0.015	0.421 $\pm$ 0.016	0.488 $\pm$ 0.014
MAS-Del $\downarrow$	<b>0.264<math>\pm</math>0.010</b>	0.395 $\pm$ 0.010	0.373 $\pm$ 0.008	0.359 $\pm$ 0.007	0.320 $\pm$ 0.010	0.359 $\pm$ 0.011	0.314 $\pm$ 0.011	0.325 $\pm$ 0.004
<i>Causal faithfulness (normalized, blur)</i>								
Ins-AUC $\uparrow$	<b>0.492<math>\pm</math>0.016</b>	0.347 $\pm$ 0.013	0.404 $\pm$ 0.016	0.430 $\pm$ 0.014	0.448 $\pm$ 0.014	0.415 $\pm$ 0.014	0.369 $\pm$ 0.013	<b>0.477<math>\pm</math>0.015</b>
Del-AUC $\downarrow$	<b>0.130<math>\pm</math>0.008</b>	0.212 $\pm$ 0.010	0.164 $\pm$ 0.009	<b>0.135<math>\pm</math>0.008</b>	0.147 $\pm$ 0.008	0.178 $\pm$ 0.010	0.179 $\pm$ 0.010	<b>0.122<math>\pm</math>0.007</b>
<i>Map focus and local robustness</i>								
Sparseness $\uparrow$	0.706 $\pm$ 0.002	0.504 $\pm$ 0.007	0.450 $\pm$ 0.002	0.497 $\pm$ 0.002	0.649 $\pm$ 0.002	0.608 $\pm$ 0.003	<b>0.714<math>\pm</math>0.002</b>	0.513 $\pm$ 0.002
Infidelity $\downarrow$	<b>0.058<math>\pm</math>0.008</b>	<b>0.057<math>\pm</math>0.008</b>	0.432 $\pm$ 0.017	$3.81 \times 10^3 \pm 1.32 \times 10^2$	0.077 $\pm$ 0.008	0.104 $\pm$ 0.009	<b>0.057<math>\pm</math>0.008</b>	<b>0.057<math>\pm</math>0.008</b>

Table 9: Quantitative evaluation on ResNet-50. Values are dataset-level mean $\pm$ 95% confidence intervals. We report only blur-based metrics for attribution calibration and causal faithfulness. Abbreviations: AGI = Adversarial IG, SG = SmoothGrad. The best result in each row is shown in **bold**; methods whose confidence intervals overlap with the best are shown in **bold**.

Metric	FRInGe (Ours)	AGI	GGIG	GeoIG	GuidedIG	IG	IG <sup>2</sup>	SG
<i>Attribution calibration</i>								
MAS-Ins $\uparrow$	<b>0.648<math>\pm</math>0.014</b>	0.463 $\pm$ 0.015	0.491 $\pm$ 0.015	0.523 $\pm$ 0.014	0.551 $\pm$ 0.016	0.516 $\pm$ 0.015	0.492 $\pm$ 0.017	0.562 $\pm$ 0.013
MAS-Del $\downarrow$	<b>0.302<math>\pm</math>0.012</b>	0.424 $\pm$ 0.011	0.410 $\pm$ 0.011	0.379 $\pm$ 0.009	0.347 $\pm$ 0.012	0.388 $\pm$ 0.013	0.355 $\pm$ 0.013	0.323 $\pm$ 0.005
<i>Causal faithfulness (normalized, blur)</i>								
Ins-AUC $\uparrow$	<b>0.581<math>\pm</math>0.016</b>	0.423 $\pm$ 0.014	0.477 $\pm$ 0.016	0.527 $\pm$ 0.016	0.527 $\pm$ 0.015	0.481 $\pm$ 0.014	0.424 $\pm$ 0.014	<b>0.582<math>\pm</math>0.016</b>
Del-AUC $\downarrow$	<b>0.161<math>\pm</math>0.009</b>	0.257 $\pm$ 0.012	0.213 $\pm$ 0.010	0.159 $\pm$ 0.009	0.183 $\pm$ 0.010	0.226 $\pm$ 0.012	0.233 $\pm$ 0.012	<b>0.144<math>\pm</math>0.008</b>
<i>Map focus and local robustness</i>								
Sparseness $\uparrow$	0.702 $\pm$ 0.002	0.490 $\pm$ 0.006	0.463 $\pm$ 0.003	0.507 $\pm$ 0.002	0.656 $\pm$ 0.003	0.621 $\pm$ 0.003	<b>0.716<math>\pm</math>0.002</b>	0.539 $\pm$ 0.003
Infidelity $\downarrow$	<b>0.150<math>\pm</math>0.050</b>	<b>0.147<math>\pm</math>0.048</b>	2.004 $\pm$ 0.101	$5.43 \times 10^3 \pm 1.98 \times 10^2$	<b>0.175<math>\pm</math>0.047</b>	<b>0.232<math>\pm</math>0.054</b>	<b>0.148<math>\pm</math>0.050</b>	<b>0.147<math>\pm</math>0.048</b>

Table 10: Quantitative evaluation on ResNet-101. Values are dataset-level mean $\pm$ 95% confidence intervals. We report only blur-based metrics for attribution calibration and causal faithfulness. Abbreviations: AGI = Adversarial IG, SG = SmoothGrad. The best result in each row is shown in **bold**; methods whose confidence intervals overlap with the best are shown in **bold**.

Metric	FRInGe (Ours)	AGI	GGIG	GeoIG	GuidedIG	IG	IG <sup>2</sup>	SG
<i>Attribution calibration</i>								
MAS-Ins $\uparrow$	<b>0.679<math>\pm</math>0.014</b>	0.520 $\pm$ 0.014	0.555 $\pm$ 0.014	0.567 $\pm$ 0.013	0.605 $\pm$ 0.014	0.577 $\pm$ 0.014	0.569 $\pm$ 0.016	0.605 $\pm$ 0.012
MAS-Del $\downarrow$	<b>0.351<math>\pm</math>0.015</b>	0.475 $\pm$ 0.014	0.437 $\pm$ 0.013	0.414 $\pm$ 0.012	0.397 $\pm$ 0.015	0.433 $\pm$ 0.015	0.416 $\pm$ 0.016	<b>0.341<math>\pm</math>0.006</b>
<i>Causal faithfulness (normalized, blur)</i>								
Ins-AUC $\uparrow$	<b>0.641<math>\pm</math>0.017</b>	0.511 $\pm$ 0.015	0.572 $\pm$ 0.017	0.607 $\pm$ 0.016	0.602 $\pm$ 0.016	0.570 $\pm$ 0.015	0.505 $\pm$ 0.015	<b>0.646<math>\pm</math>0.016</b>
Del-AUC $\downarrow$	0.228 $\pm$ 0.012	0.315 $\pm$ 0.014	0.241 $\pm$ 0.011	0.199 $\pm$ 0.010	0.243 $\pm$ 0.013	0.278 $\pm$ 0.013	0.300 $\pm$ 0.014	<b>0.187<math>\pm</math>0.010</b>
<i>Map focus and local robustness</i>								
Sparseness $\uparrow$	0.706 $\pm$ 0.002	0.492 $\pm$ 0.006	0.482 $\pm$ 0.003	0.506 $\pm$ 0.002	0.660 $\pm$ 0.003	0.620 $\pm$ 0.003	<b>0.722<math>\pm</math>0.002</b>	0.537 $\pm$ 0.003
Infidelity $\downarrow$	<b>0.121<math>\pm</math>0.022</b>	<b>0.119<math>\pm</math>0.021</b>	1.681 $\pm$ 0.084	6.03 $\times$ 10 <sup>3</sup> $\pm$ 2.07 $\times$ 10 <sup>2</sup>	<b>0.149<math>\pm</math>0.021</b>	0.189 $\pm$ 0.022	<b>0.120<math>\pm</math>0.022</b>	<b>0.119<math>\pm</math>0.021</b>

Table 11: Quantitative evaluation on ResNet-152. Values are dataset-level mean $\pm$ 95% confidence intervals. We report only blur-based metrics for attribution calibration and causal faithfulness. Abbreviations: AGI = Adversarial IG, SG = SmoothGrad. The best result in each row is shown in **bold**; methods whose confidence intervals overlap with the best are shown in **bold**.

Metric	FRInGe (Ours)	AGI	GGIG	GeoIG	GuidedIG	IG	IG <sup>2</sup>	SG
<i>Attribution calibration</i>								
MAS-Ins $\uparrow$	<b>0.691<math>\pm</math>0.013</b>	0.537 $\pm$ 0.014	0.563 $\pm$ 0.015	0.588 $\pm$ 0.012	0.619 $\pm$ 0.015	0.588 $\pm$ 0.015	0.590 $\pm$ 0.016	0.620 $\pm$ 0.012
MAS-Del $\downarrow$	0.392 $\pm$ 0.017	0.500 $\pm$ 0.015	0.469 $\pm$ 0.015	0.432 $\pm$ 0.014	0.419 $\pm$ 0.016	0.463 $\pm$ 0.016	0.442 $\pm$ 0.018	<b>0.349<math>\pm</math>0.007</b>
<i>Causal faithfulness (normalized, blur)</i>								
Ins-AUC $\uparrow$	<b>0.681<math>\pm</math>0.016</b>	0.538 $\pm$ 0.016	0.592 $\pm$ 0.017	0.651 $\pm$ 0.016	0.631 $\pm$ 0.015	0.587 $\pm$ 0.015	0.539 $\pm$ 0.015	<b>0.682<math>\pm</math>0.015</b>
Del-AUC $\downarrow$	0.265 $\pm$ 0.013	0.358 $\pm$ 0.015	0.301 $\pm$ 0.013	0.229 $\pm$ 0.012	0.275 $\pm$ 0.013	0.324 $\pm$ 0.015	0.343 $\pm$ 0.014	<b>0.215<math>\pm</math>0.011</b>
<i>Map focus and local robustness</i>								
Sparseness $\uparrow$	0.703 $\pm$ 0.002	0.496 $\pm$ 0.006	0.490 $\pm$ 0.003	0.510 $\pm$ 0.002	0.661 $\pm$ 0.003	0.624 $\pm$ 0.003	<b>0.726<math>\pm</math>0.002</b>	0.546 $\pm$ 0.003
Infidelity $\downarrow$	<b>0.111<math>\pm</math>0.020</b>	<b>0.111<math>\pm</math>0.019</b>	2.539 $\pm$ 0.134	6.29 $\times$ 10 <sup>3</sup> $\pm$ 2.25 $\times$ 10 <sup>2</sup>	<b>0.142<math>\pm</math>0.020</b>	0.192 $\pm$ 0.021	<b>0.110<math>\pm</math>0.019</b>	<b>0.111<math>\pm</math>0.019</b>

Table 12: Quantitative evaluation on VGG-19. Values are dataset-level mean $\pm$ 95% confidence intervals. We report only blur-based metrics for attribution calibration and causal faithfulness. Abbreviations: AGI = Adversarial IG, SG = SmoothGrad. The best result in each row is shown in **bold**; methods whose confidence intervals overlap with the best are shown in **bold**.

Metric	FRInGe (Ours)	AGI	GGIG	GeoIG	GuidedIG	IG	IG <sup>2</sup>	SG
<i>Attribution calibration</i>								
MAS-Ins $\uparrow$	<b>0.588<math>\pm</math>0.015</b>	0.440 $\pm$ 0.014	0.460 $\pm$ 0.015	0.487 $\pm$ 0.014	0.496 $\pm$ 0.015	0.479 $\pm$ 0.015	0.448 $\pm$ 0.017	0.523 $\pm$ 0.014
MAS-Del $\downarrow$	<b>0.255<math>\pm</math>0.008</b>	0.405 $\pm$ 0.009	0.357 $\pm$ 0.008	0.335 $\pm$ 0.006	0.305 $\pm$ 0.009	0.337 $\pm$ 0.010	0.290 $\pm$ 0.010	0.304 $\pm$ 0.004
<i>Causal faithfulness (normalized, blur)</i>								
Ins-AUC $\uparrow$	<b>0.503<math>\pm</math>0.016</b>	0.448 $\pm$ 0.016	0.441 $\pm$ 0.016	0.490 $\pm$ 0.015	0.468 $\pm$ 0.015	0.450 $\pm$ 0.014	0.419 $\pm$ 0.015	<b>0.522<math>\pm</math>0.016</b>
Del-AUC $\downarrow$	<b>0.119<math>\pm</math>0.007</b>	0.192 $\pm$ 0.010	0.159 $\pm$ 0.008	0.118 $\pm$ 0.007	0.148 $\pm$ 0.008	0.170 $\pm$ 0.009	0.159 $\pm$ 0.009	<b>0.113<math>\pm</math>0.007</b>
<i>Map focus and local robustness</i>								
Sparseness $\uparrow$	0.707 $\pm$ 0.003	0.433 $\pm$ 0.006	0.497 $\pm$ 0.003	0.529 $\pm$ 0.002	0.674 $\pm$ 0.003	0.637 $\pm$ 0.003	<b>0.765<math>\pm</math>0.003</b>	0.547 $\pm$ 0.003
Infidelity $\downarrow$	<b>0.343<math>\pm</math>0.064</b>	<b>0.346<math>\pm</math>0.064</b>	0.862 $\pm$ 0.065	4.27 $\times$ 10 <sup>3</sup> $\pm$ 1.86 $\times$ 10 <sup>2</sup>	<b>0.387<math>\pm</math>0.063</b>	<b>0.419<math>\pm</math>0.066</b>	<b>0.342<math>\pm</math>0.064</b>	<b>0.342<math>\pm</math>0.064</b>

### D.3 Robustness under small input perturbations

We additionally report Max Sensitivity as a direct robustness diagnostic under small input perturbations, evaluated on a sample of 64 images for each architecture. Because this metric is defined through a maximum over sampled perturbations and can therefore be skewed by a small number of difficult examples, we summarize it here using the median together with the interquartile half-width, i.e.,  $(Q_3 - Q_1)/2$ . This yields a robust summary of central tendency and dispersion that is less sensitive to outliers than the mean.

Table 13 shows that FRInGe does not exhibit systematically unstable behavior relative to standard IG. In particular, FRInGe attains lower median Max Sensitivity on ResNet-18 and VGG-19, while IG is lower on ResNet-50, ResNet-101, ResNet-152, and Inception-v3. At the same time, FRInGe often yields a comparatively concentrated spread across images, indicating that its local sensitivity remains controlled on several architectures. We therefore interpret Max Sensitivity as a complementary robustness diagnostic: it does not show uniform dominance of FRInGe over IG, but neither does it indicate a systematic robustness failure induced by the geometry-aware construction.

Table 13: Max Sensitivity across architectures for FRInGe and standard IG, evaluated on a sample of 64 images per model. Values are reported as median  $\pm$  half-IQR, where half-IQR =  $(Q_3 - Q_1)/2$ . Lower is better. The best median in each row is shown in **bold**; methods whose median  $\pm$  half-IQR intervals overlap with the best are shown in **bold** as a descriptive near-tie heuristic.

Model	FRInGe	IG
ResNet-18	<b>0.0758 <math>\pm</math> 0.0122</b>	<b>0.0833 <math>\pm</math> 0.0171</b>
ResNet-50	<b>0.1139 <math>\pm</math> 0.0141</b>	<b>0.0917 <math>\pm</math> 0.0313</b>
ResNet-101	0.1225 $\pm$ 0.0138	<b>0.0829 <math>\pm</math> 0.0209</b>
ResNet-152	0.1383 $\pm$ 0.0170	<b>0.0900 <math>\pm</math> 0.0313</b>
Inception-v3	0.1081 $\pm$ 0.0131	<b>0.0381 <math>\pm</math> 0.0093</b>
VGG-19	<b>0.0665 <math>\pm</math> 0.0094</b>	<b>0.0678 <math>\pm</math> 0.0126</b>

## E Additional Qualitative Results

We further compare attribution maps qualitatively across all methods on a small set of automatically selected images. To make the selection reproducible, we rank images using an image-level dominance score based on the same four metrics used in the quantitative evaluation, while assigning greater weight to the MAS criteria in order to foreground calibration behavior. We additionally retain only examples for which FRInGe outperforms most competing methods on both MAS-Insertion and MAS-Deletion. These examples are therefore not arbitrary visual anecdotes, but targeted illustrations of the cases where FRInGe’s distribution-space trajectory yields the clearest practical benefit.

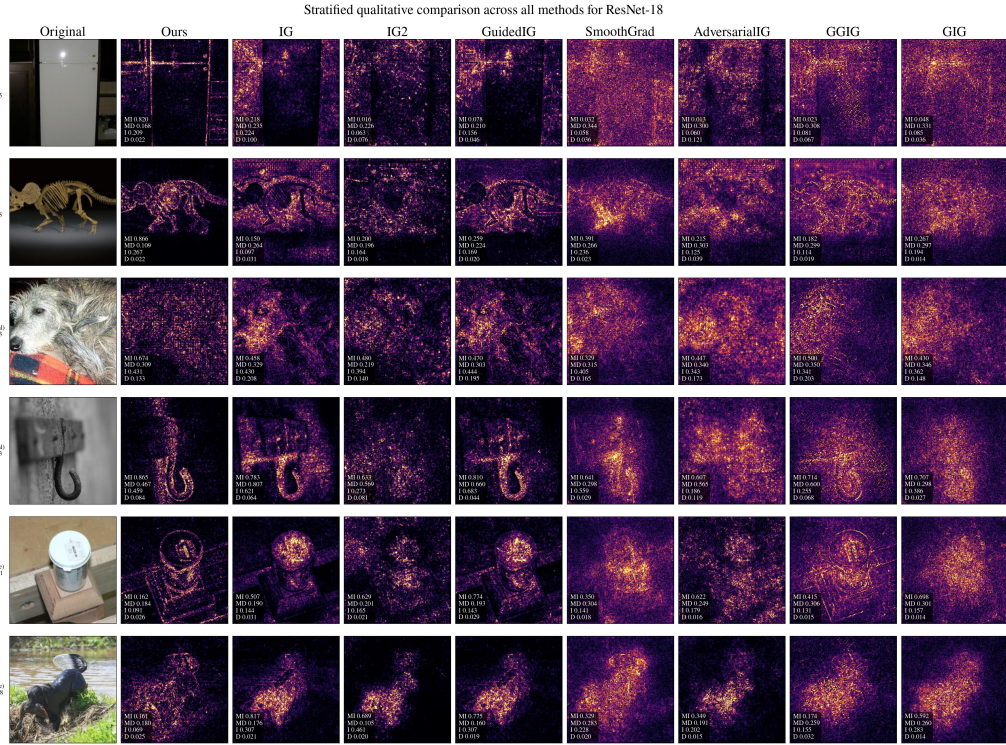


Figure 12: Qualitative comparison across all attribution methods on ResNet-18. Images are selected automatically using the image-level dominance score described in the text.

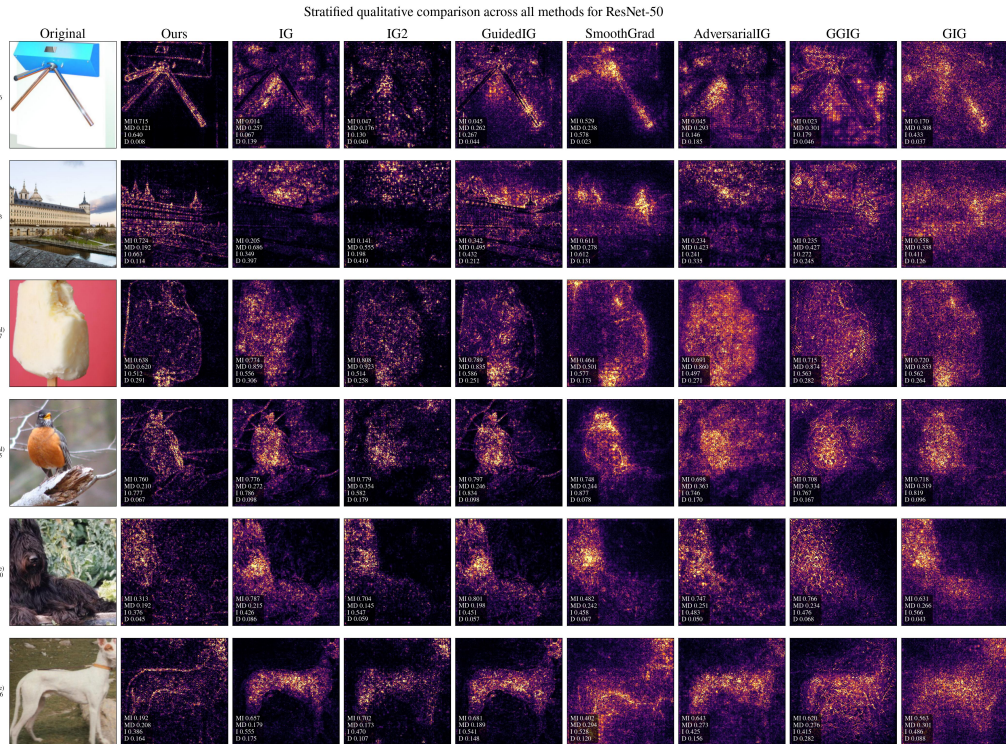


Figure 13: Qualitative comparison across all attribution methods on ResNet-50. Images are selected automatically using the image-level dominance score described in the text.

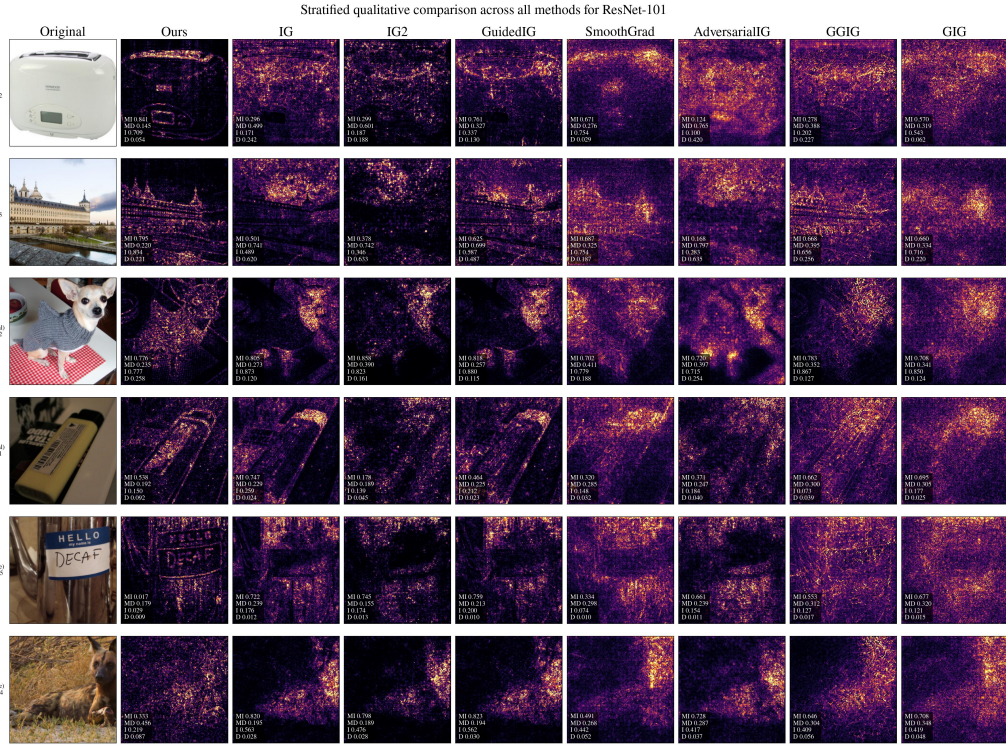


Figure 14: Qualitative comparison across all attribution methods on ResNet-101. Images are selected automatically using the image-level dominance score described in the text.

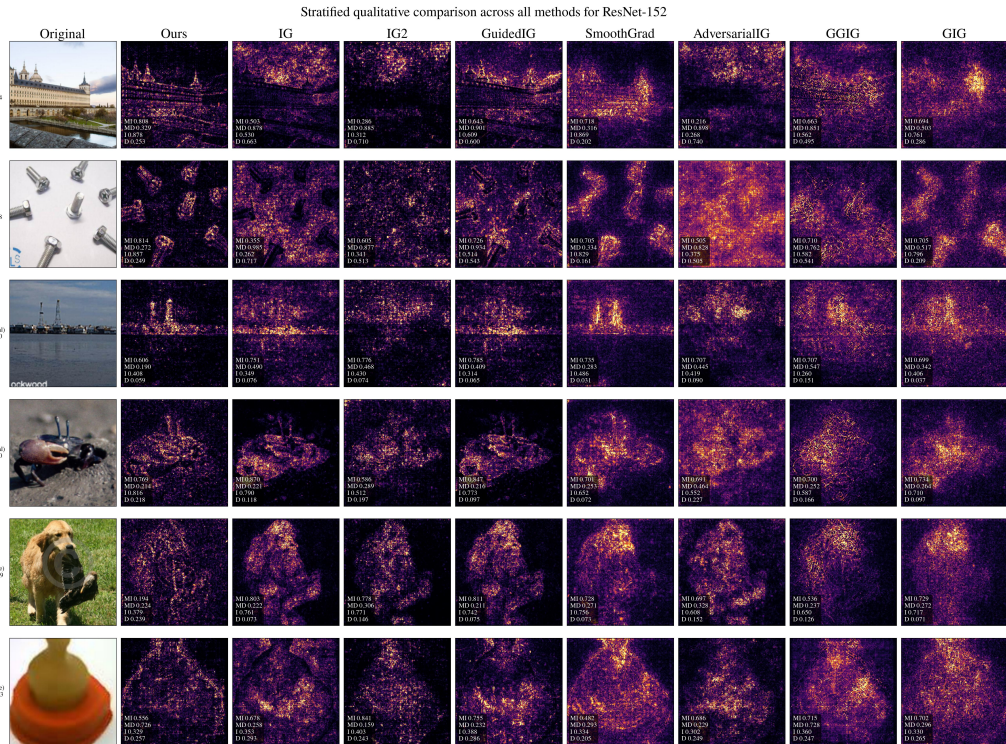


Figure 15: Qualitative comparison across all attribution methods on ResNet-152. Images are selected automatically using the image-level dominance score described in the text.

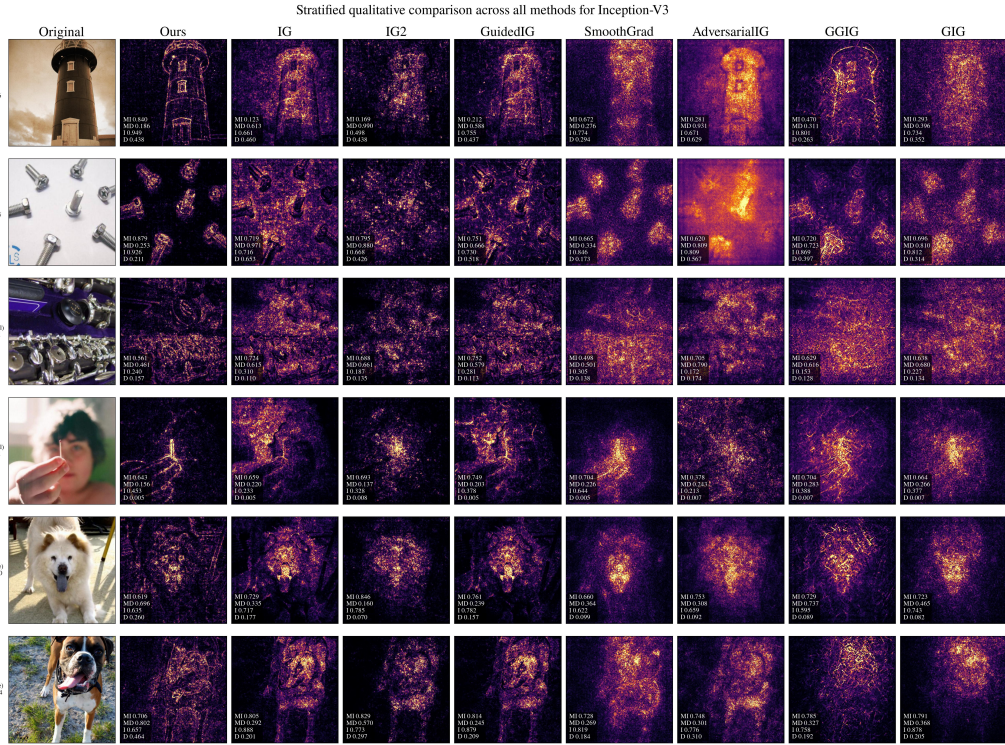


Figure 16: Qualitative comparison across all attribution methods on Inception-V3. Images are selected automatically using the image-level dominance score described in the text.

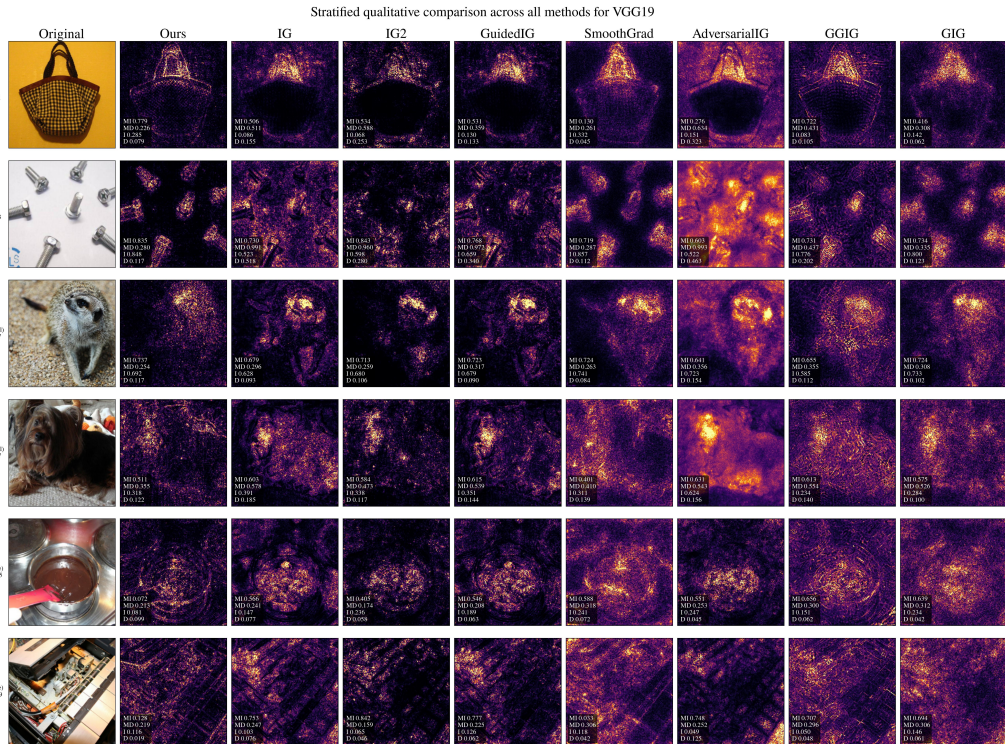


Figure 17: Qualitative comparison across all attribution methods on VGG-19. Images are selected automatically using the image-level dominance score described in the text.